Chapter 1

Introduction

1.1 Optical imaging

The desire to preserve moments in everyone's life drives the need for advanced optical systems that can record scenes as images. "Imaging," which comes from the concept of "writing with light," is the process of creating two-dimensional (2D) representations of objects. The fundamental idea involves the interaction of light with an object to encode the object's information in the fundamental features of light, such as amplitude, phase, and polarization [1,2]. These fundamental features allow us to sense the reflectivity, thickness distributions, birefringence, and various other characteristics of objects [3]. The object characteristics imprinted on the light scatters in various directions, and the goal is to measure the changes in the characteristics of light after interaction with the object using optical detection devices. Depending on the detection mechanism, optical imaging can be roughly divided into qualitative and quantitative categories. While qualitative imaging, such as the human eye, relies on subjective interpretation, quantitative imaging utilizes advanced sensors, such as charge-coupled devices (CCD) or complementary metal oxide semiconductors (CMOS), for precious measurements.

In optical physics, a coherent light field is represented as a complex field characterized by amplitude and phase distributions. Among these, phase is a crucial parameter as it contains important information and governs the propagation properties of light. Traditional optical detectors measure only the intensity, which is equivalent to the optical power, and phase information is missing. This directly measured intensity is related to the complex optical field as follows.

Consider a complex field of the light field at position $\boldsymbol{r}$ and time t as

$$U(\boldsymbol{r},t)=U_0(\boldsymbol{r},t)\exp[i\varphi(\boldsymbol{r},t)] \tag{1.1}$$

where $U_0(\boldsymbol{r},t)$ indicates the amplitude distribution of the light and φ represents the spatial phase distribution. Using the key points as discussed in Ref. [4], the intensity of a scalar monochromatic wave at a point $\boldsymbol{r}$, at a particular instant of time t is mathematically expressed as

$$I(\boldsymbol{r},t)=|U_0(\boldsymbol{r},t)|^2 \tag{1.2}$$

For a sake of brevity, we have ignored time t in the coming section. Although intensity is directly measurable attribute of the optical field, its phase information is lost, which carries significant information about the light field. This phenomenon, commonly known as "phase loss", poses a challenge in optical imaging.

Fig. 1.1 illustrates a plane wavefront incident on a phase object, then through an optical imaging system, and the resulting intensity pattern is captured through a CCD/CMOS detector. Over the years, researchers have recognized that phase variation carries more valuable information than amplitude variations [5–7]. Extracting the phase information from intensity measurements is termed as quantitative phase imaging problem and has been extensively studied due to its profound applications. [8,9]. These applications span across various domains such as X-ray crystallography [10–16], electron microscopy [17,18], biological imaging [19], astronomical imaging [20–23], etc.

In quantitative optical imaging, phase measurement is pivotal for recovering complete object information. For instance, transparent biological cells, fog, atmospheric turbulence, etc., predominantly modulate the phase of transmitted light. These phase variations arising due to refractive index fluctuations contain valuable information about the object.

Similarly, when a polarized light interacts with an object, the polarization of light becomes another key degree of freedom that carries additional information of the object,

such as birefringence, surface properties, color contrast, etc. [24–27]. Polarization describes the oscillation direction of light's electric field vector and provides unique insights into the properties of the object that are otherwise invisible through intensity measurement with the detector. Control over polarization has enabled breakthroughs in imaging, sensing, metrology, and non-destructive evaluation, allowing for enhanced detection of inner structures or subtle surface variations [28–33].

To connect quantitative imaging with coherent light and later with correlation of coherent random fields, some major contributions in quantitative imaging is briefly covered in the coming section.

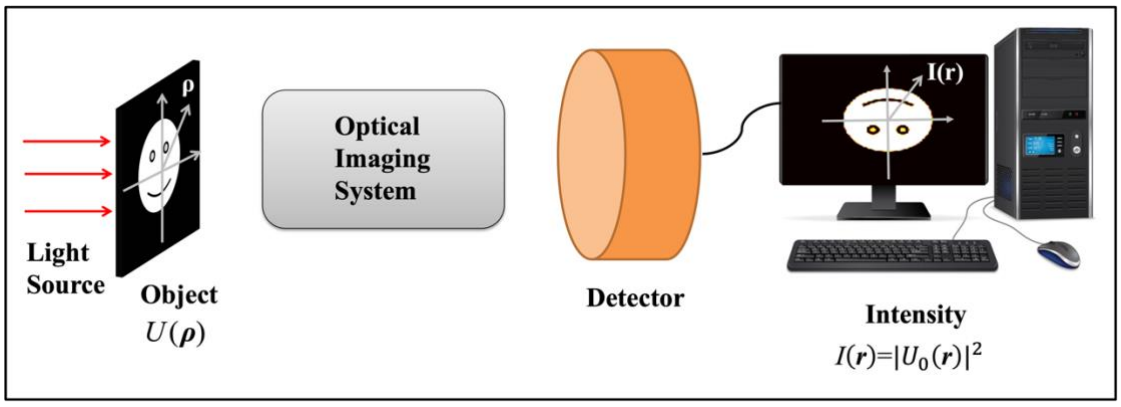

Fig. 1.1 Imaging configuration.

1.2 Quantitative phase imaging

In optical imaging, phase recovery at optical frequencies is an indirect process since only intensity of light is a directly measurable quantity with optical detectors. The primary objective of phase imaging methodologies is to deduce phase information from the measured intensity data. To address this challenge, both iterative and non-iterative phase recovery techniques have been developed.

Phase contrast microscopy, introduced by Zernike, is one of the earliest methods to visualize phase variations [34,35]. It employs a phase mask to transform phase derivatives into intensity patterns, yielding qualitative phase information suitable for visualization. Nevertheless, this approach is limited to visual aids only and is not effective in delivering quantitative phase data. The advent of Laser revolutionized phase recovery using holography, allowing quantitative phase estimation by recording the interference of the unknown object field with a mutually coherent known reference field [36–39]. Despite its great effectiveness, holography typically requires complex experimental setups. As an alternative, non-interferometric approaches have been developed to infer phase from one or more intensity measurements using wavefront propagation or transformations through optical systems. Interestingly, far-field propagation of optical field corresponds to the Fourier transform of the object transmission function. This characteristic serves as the basis of iterative phase retrieval techniques. In the next section, some non-iterative and iterative phase recovery are discussed.

1.2.1 Non-iterative phase imaging

Non-iterative methods have been applied to recover phase from intensity measurements in several cases of pure-phase, small-phase, or homogeneous objects [40,41]. Some notable techniques in this category are discussed below.

1.2.1.1 Holography

Holography plays a significant role in imaging by making it possible to record and reconstruct the complex field, including both amplitude and phase [42–44]. Initially introduced by Gabor in 1948 and further advanced by Leith and Upatneiks in the 1960s, holography encodes amplitude and phase information into an interference pattern, named as hologram, by combining the unknown optical field with a reference wave. Availability

of digital recording devices and numerical reconstruction of the hologram has led to the development of digital holography (DH) technique [45–50]. This development has made remarkable progress in the quantitative phase imaging using DH. DH can be implemented using various geometries, and vital among them are in-line [42], off-axis [43], and phase-shifting [51,52], as depicted in Fig. 1.2.

Consider an interference of coherent waves coming from an object $U_o(\boldsymbol{r})$ and reference $R(\boldsymbol{r})$ at the detection plane as shown in Fig. 1.18. The intensity at the observation plane is denoted as

$$I(\boldsymbol{r}) = |U_o(\boldsymbol{r}) + R(\boldsymbol{r})|^2 \tag{1.3}$$

Eq. (1.3) can be written as

$$I(\boldsymbol{r}) = |U_o(\boldsymbol{r})|^2 + |R(\boldsymbol{r})|^2 + U_o(\boldsymbol{r})R^*(\boldsymbol{r}) + U_o^*(\boldsymbol{r})R(\boldsymbol{r}), \tag{1.4}$$

where asterisk * indicates the complex conjugate and ***I(r)*** represents the hologram. It consists of three terms: the 0-order is composed of $|U_o(\boldsymbol{r})|^2 + |R(\boldsymbol{r})|^2$, the +1 order is represented by $U_o(\boldsymbol{r})R^*(\boldsymbol{r})$, and the -1 order is $U_o^*(\boldsymbol{r})R(\boldsymbol{r})$.

The in-line holography involves direct interference between the object and reference beams as shown in Fig. 1.2 (a). However, the overlapping of 0-order, +1 order, and -1 order terms in the hologram corresponding to different components in Eq. (1.4) create a twin image problem along with a strong background. This issue is mitigated by providing an angular separation between the object and reference beam in the off-axis holography, as represented in Fig. 1.2 (b). Nevertheless, off-axis holography is constrained by the limited pixel size of digital sensors, which restricts the available frequency space and

field of view (FOV) [53]. To address the limitations of off-axis holography, phase-shifting holography has been proposed as depicted in Fig. 1.2 (c). Phase-shifting holography records multiple holograms with phase shifts between the object and reference beams. The phase shifts are introduced using devices like a piezoelectric transducer [52], liquid crystal phase modulator [54], or an acousto-optic modulator [55]. This technique resolves the issue of off-axis holography, and expands the FOV [56,57].

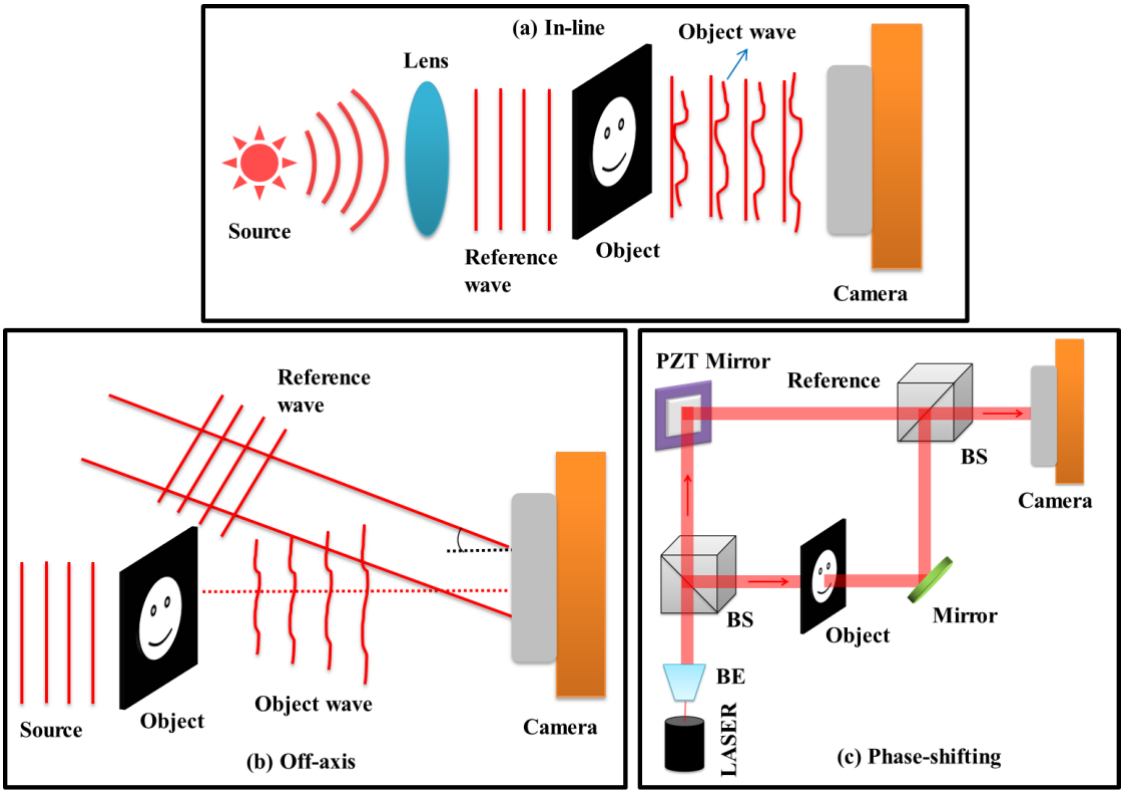

Fig. 1.2 Basic geometries for holography.

In recent years, deep learning has also emerged as a powerful tool in coherent imaging [58–61]. Furthermore, deep learning-based methods have opened new frontiers in quantitative phase imaging, leveraging computational techniques to enhance the accuracy and efficiency of phase retrieval.

Additionally, compact and stable digital holography setups have been developed using common-path geometries, further simplifying experimental requirements while maintaining robustness [62–65]. These advancements continue to expand the applicability of digital holography across diverse fields.

1.2.1.2 Kramers-Kronig (KK) relations

In addition to holography-based techniques, non-interferometric phase imaging, free from iterative algorithms, simplifies imaging setup by removing interferometric geometry. The Kramers–Kronig (KK) relations, a mathematical formulation connecting the real and imaginary parts of a complex function, serves as one of the domains for developing these phase imaging techniques. In phase imaging, the real part of the complex object is captured through a digital sensor. The corresponding phase information is then deduced using the KK [66–68]. In the spatial domain, the KK relations ensure that the Fourier components of the reconstructed signal meet the analytic signal criteria. Baek et. al. demonstrated this concept by employing space-domain KK relations to recover phase from a single intensity measurement under oblique illumination [67]. The schematic of the experimental setup is illustrated in Fig. 1.3. The KK relation works on the basis of connecting real and imaginary parts of a complex function. A square-integrable function *f(x)* that is analytic in the upper half-plane of *x* satisfies the equation

$$\mathrm{Im}\left[f(x)\right] = -\frac{1}{\pi} P \int_{-\infty}^{\infty} \frac{\mathrm{Re}\left[f(x')\right]}{x'-x} dx', \tag{1.5}$$

where *P* indicates the Cauchy principal value. KK relations apply to the logarithm of the complex field $U(\boldsymbol{r})$ whose real and imaginary parts are

$$\mathrm{Re}\left[\log(U(\boldsymbol{r}))\right] = \log(I(\boldsymbol{r}))/2, \tag{1.6}$$

$$\mathrm{Im}\left[\log(U(\boldsymbol{r}))\right] = \arg(U(\boldsymbol{r})), \tag{1.7}$$

where, $I(\boldsymbol{r}) = \left|U(\boldsymbol{r})\right|^2$, the real part corresponds to the intensity, while the imaginary part represents the phase. Thus, the phase image can be recovered from intensity image without requiring iterative algorithms or strict constraints.

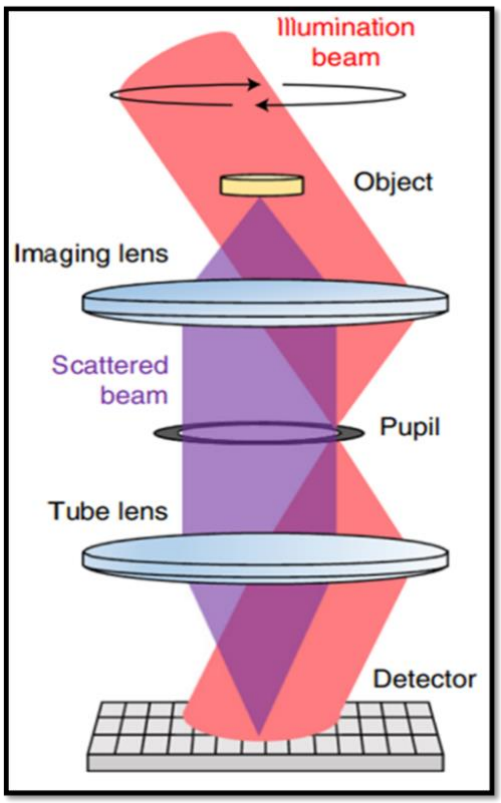

Fig. 1.3 Schematic of experimental setup of phase imaging with KK relations [67].

KK relations-based approach requires less raw data as well as processing time and provides a robust and computationally efficient framework for phase recovery, especially in scattering or complex imaging environments.

1.2.1.3 Transport of Intensity Equation (TIE)

Transport of Intensity Equation (TIE) presents another interesting non-iterative approach for phase imaging. It provides a simple experimental framework for quantitative phase

measurements by relating phase data at the in-focus plane to the axial derivative of intensity distribution [69–74]. The TIE, rooted in the principle of conservation of energy, has broad applications beyond optics, such as transmission electron microscopy (TEM) [75], neutron imaging [76], measurement of quantum-mechanical wave-fields [77], electron microscopy [78] etc.

Teague proposed that the phase of a wavefront could be determined by measuring the intensity derivative along the optical axis in Fresnel region and then solving a partial differential equation known as TIE [79]. An experimental setup for TIE based imaging is shown in Fig. 1.4. A beam is collimated by a lens and the collimated beam illuminates the object. The complex field of the object traveling in $+z$ direction can be expressed as:

$$U(\boldsymbol{r}) = \sqrt{I(\boldsymbol{r})}\exp\left[i\varphi(\boldsymbol{r})\right] \tag{1.8}$$

where, $I(\boldsymbol{r})$ represents intensity and $\varphi(\boldsymbol{r})$ is phase of the wavefront.

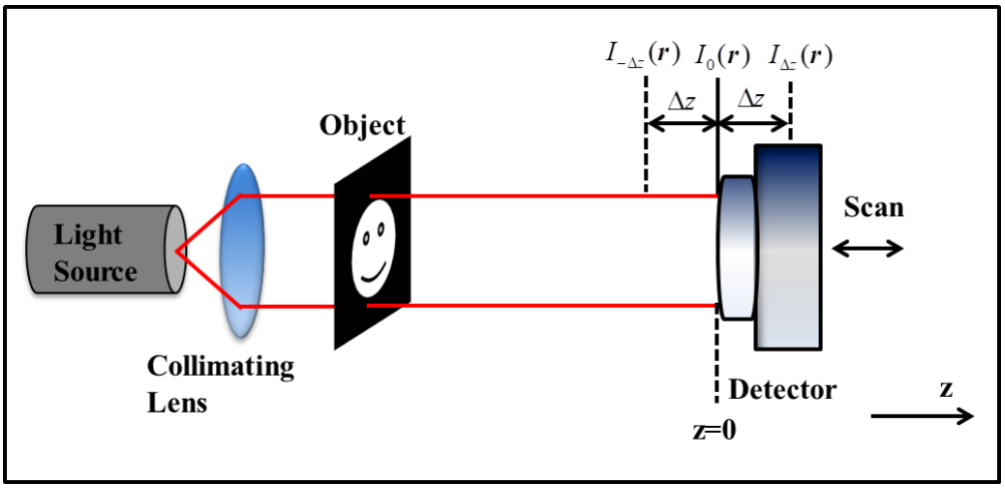

Fig. 1.4 The optical setup for TIE [74].

A monochromatic optical field propagating in free space obeys the Helmholtz equation and is mathematically represented as

$$(\nabla^2 + k^2)U(\boldsymbol{r}) = 0, \tag{1.9}$$

where, ∇^2 indicates the Laplacian operator, $k = \frac{2\pi}{\lambda}$ is the propagation constant, and λ is the wavelength of the light. The complex amplitude of the coherent beams must obey the Helmholtz equation. In the paraxial approximation, the paraxial Helmholtz equation is represented as

$$\nabla^2 U(\boldsymbol{r}) + 2jk\frac{\partial U(\boldsymbol{r})}{\partial z} = 0, \tag{1.10}$$

Substituting the complex scalar field $U(\boldsymbol{r})$ from Eq. (1.8) into Eq. (1.10), simplifies the TIE as

$$-k\frac{\partial I(\boldsymbol{r})}{\partial z} = \nabla \cdot \left[I(\boldsymbol{r}) \nabla \varphi(\boldsymbol{r}) \right]. \tag{1.11}$$

It is a second-order elliptical partial differential equation about the phase function $\varphi(\boldsymbol{r})$. The image sensor plane is set at z=0 and solves the TIE for phase using Fourier transform [74] as

$$\varphi(\boldsymbol{r}) = -kIFT\left[\frac{1}{4\pi^2(u^2+v^2)} FT\left[\nabla . \frac{\nabla}{I_0(\boldsymbol{r})} \times IFT\left[\frac{1}{4\pi^2(u^2+v^2)} FT\left[\frac{\partial I_0(\boldsymbol{r})}{\partial z}\right]\right]\right]\right], \tag{1.12}$$

where, u and v are the spatial frequencies corresponding to x and y directions, respectively. The operators FT and IFT indicate Fourier and inverse Fourier transforms, respectively. The intensity derivative in the right-hand side of the above Eq. is approximated by the difference of two intensity distributions at different depth positions Δz and $-\Delta z$

$$\frac{\partial I_0(\boldsymbol{r})}{\partial z} = \frac{I_{\Delta z}(\boldsymbol{r}) - I_{-\Delta z}(\boldsymbol{r})}{2\Delta z}. \tag{1.13}$$

The phase distribution is recovered by substituting experimentally recorded three intensities, i.e., in Eqs. (1.12) and (1.13). Finally, the complex field in the image plane is obtained from the intensity and the phase. One advantage of TIE is that it eliminates the need for phase unwrapping, simplifying the phase retrieval process. However, the necessity to measure intensity at multiple planes imposes certain limitations in experimental implementation.

1.2.1.4 Wavefront sensing

Wavefront sensing techniques aim to recover the phase. The Shack–Hartmann wavefront sensor is one of the most widely used methods due to its robust design and capability to enhance image quality [80–82]. A Shack-Hartman wavefront sensor consists of an array of microlenses (also known as lenslets), where each lenslet focuses light onto a digital sensor placed in the system's focal plane. This digital sensor captures the local tilts of the wavefront and analyzes the focus spot positions. Any phase change can be approximated to a set of discrete tilts. These tilts are used to reconstruct the overall phase of the wavefront. Figure 1.5 shows the working principle of the Shack-Hartmann wavefront sensor.

The disadvantage of the Shack-Hartmann wavefront sensor method is that the spatial resolution of the wavefront is limited by the size and number of lenses. Accurate phase recovery is possible when the lenslets are much larger than the detector's pixel size.

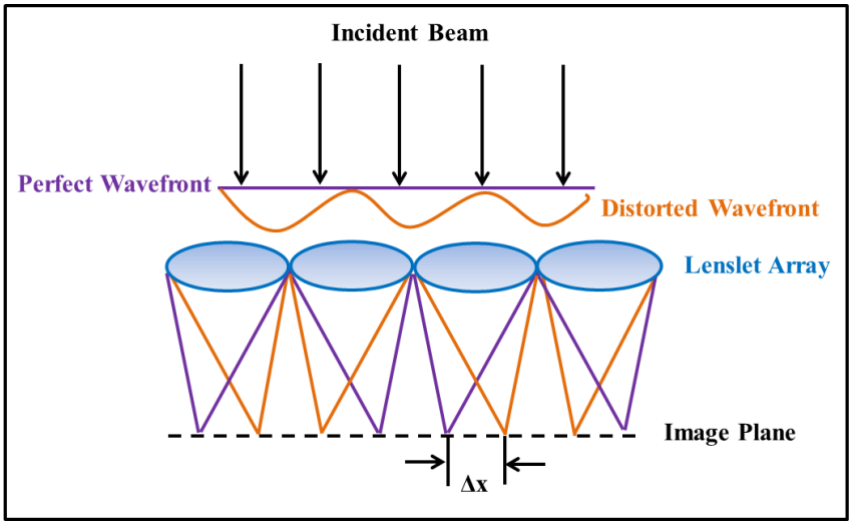

Fig. 1.5 Basic principle of phase measurement using Shack-Hartmann wavefront sensor [80].

1.2.2 Iterative phase imaging

Over several decades, iterative computational phase imaging techniques have been developed. These methods rely on iterative computation to enforce constraints in object and Fourier domains, based on intensity images at the sample and detector plane, to address the phase retrieval problem. A key advantage of iterative phase retrieval methods is their ability to perform using simpler optical systems. Gerchberg-Saxton (GS) and Fienup's algorithms are the most significant among these methods.

Initial work by Gerchberg-Saxton and later by Fienup, focused on retrieving phase using a single Fourier intensity measurement. The iterative process applies suitable support constraints in the object and Fourier domain to reconstruct the phase [83–89]. Support constraints refer to points in the object where the intensity is non-zero. It is widely recognized that the choice of support constraints influences the convergence of these algorithms. Phase retrieval algorithms with prior knowledge of support constraints demonstrate effective convergence for relatively simpler objects. Moreover, adding a non-negativity allows good support, aiding in phase reconstruction. Researchers found

that an object's autocorrelation can also be used to estimate support constraints [90]. However, phase reconstruction becomes more difficult for complex-valued or phase-only objects [91–93].

Beyond the GS and Fienup algorithms, numerous iterative techniques have been developed in recent years [94–112]. The following section explores some of the popular iterative phase retrieval techniques.

1.2.2.1 Gerchberg-Saxton (GS) algorithm

The Gerchberg–Saxton (GS) algorithm, proposed by R. W. Gerchberg and W. O. Saxton, is a pioneering iterative approach for phase retrieval. This approach determines a complex object's amplitude and phase information by iteratively approximating between the object and the Fourier domain. Using measured intensity in the Fourier domain, the algorithm iteratively refines the phase by applying suitable constraints to reconstruct the unknown phase. This approach is also known as the error-reduction algorithm because the squared error, defined as the sum of the squared differences between the iteratively calculated and experimentally measured amplitudes in the Fourier domain, decreases with each iteration.

The GS algorithm requires adequate sampling of the Fourier amplitude for accurate reconstruction [83]. Fig. 1.6 schematically shows the basic iterative procedure of the algorithm.

GS algorithm begins with the measured Fourier modulus $\left|U(\boldsymbol{r})\right|$ of an unknown object, which is calculated by taking the square root of the measured intensity $\left|U(\boldsymbol{r})\right|^2$ and a random phase function $\varphi_0(\boldsymbol{r})$ where the values of the phase functions are chosen from random distribution in the range $[-\pi, \pi]$ as an initial guess. The iterative can be summarized as follows:

1. The Fourier modulus combines the random initial phase to form a complex-valued function $U(\boldsymbol{r}) = |U(\boldsymbol{r})| \exp(i\varphi_0(\boldsymbol{r}))$. $U(\boldsymbol{r})$ is then inverse Fourier transformed to the object domain to obtain $U(\boldsymbol{\rho})$.

2. Object domain constraints, i.e. prior information about the object is applied to the $U_n(\boldsymbol{\rho})$ to obtain the modified object estimate $U_{n+1}(\boldsymbol{\rho})$.

3. The modified object estimate, $U_{n+1}(\boldsymbol{\rho})$ is Fourier transformed back to the Fourier domain to obtain $U_{n+1}(\boldsymbol{r})$. Here is the updated phase of the function $U_{n+1}(\boldsymbol{r})$ is retained while the amplitude is replaced by measured Fourier modulus $|U(\boldsymbol{r})|$.

4. Error is calculated using the relative L^2-norm of updated and measured Fourier modulus data in each iteration as,

$$E_n = \frac{\left\| |U_n(\boldsymbol{r})| - |U(\boldsymbol{r})| \right\|}{\left\| U(\boldsymbol{r}) \right\|}, \tag{1.14}$$

where ||…….|| represent L^2-norm. This iterative process continues until the error falls below a certain threshold.

Despite its historical importance, the GS algorithm convergence is slow and highly dependent on the prior knowledge object's support. Wrong guesses about the support can lead to stagnation problems, preventing meaningful solutions. The inclusion of a non-negativity constraint improves convergence rates but does not eliminate the possibility of the algorithm becoming stuck at local minima, failing to reach the true phase solution.

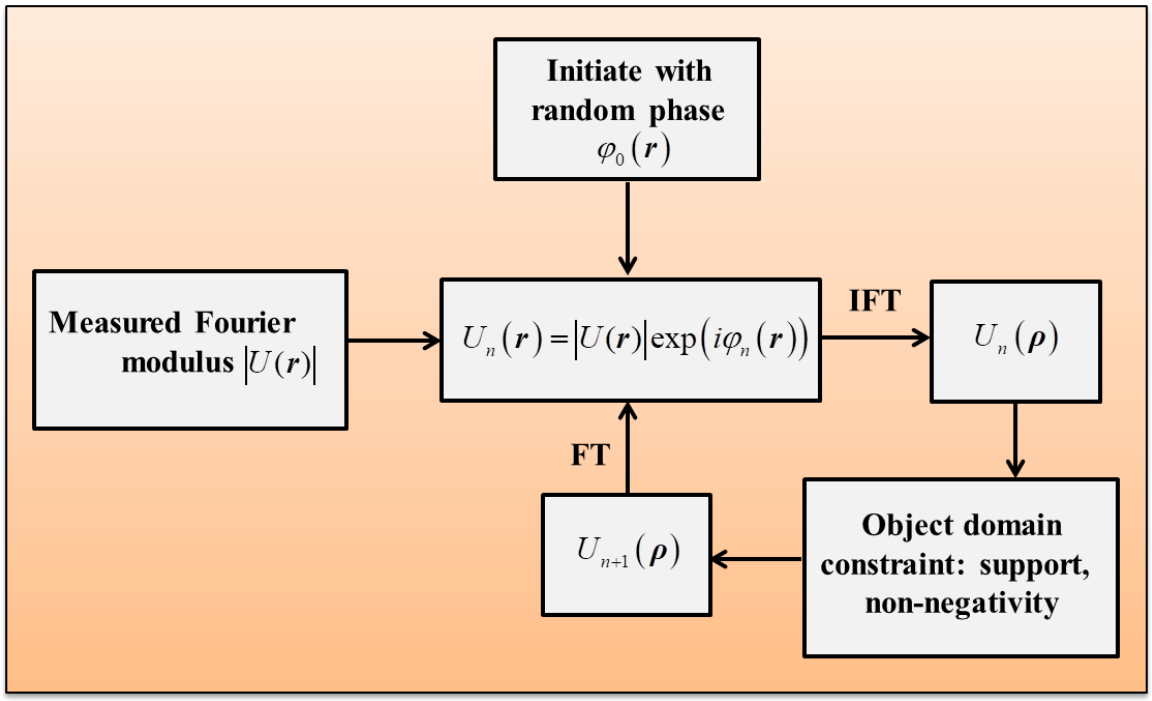

Fig. 1.6 Schematic diagram of the iterative process of GS algorithm [83].

1.2.2.2 Fienup algorithm

To overcome the limitations of the GS algorithm, J. R. Fienup introduced the Hybrid Input-Output (HIO) algorithm. This is an advanced version of the error-reduction method, which introduces a negative feedback mechanism to improve convergence and handle stagnation issues [84–89]. Unlike the GS method, which sets pixels violating object-domain constraints to zero, the HIO algorithm adjusts these pixels using a feedback term, making it more effective for complex grayscale objects.

A schematic diagram of Fienup's HIO algorithm is shown in Fig. 1.7. Iterative steps of the HIO algorithm are as follows:

1. Algorithm starts with measured Fourier modulus $|U(\boldsymbol{r})|$ and a randomly assuming phase function $\varphi_0(\boldsymbol{r})$ with values of phase in the range [$-\pi$, π], to form a complex-valued function, $U(\boldsymbol{r})$.

2. This complex function is inverse Fourier transformed to the object domain, yielding an estimate of the object, $U_n(\boldsymbol{\rho})$.

3. Object domain constraints (e.g. positivity, size /support) are applied on $U_n(\boldsymbol{\rho})$. Pixels satisfying the constraints (denoted as C) remain unchanged, while pixels violating the constraints are updated using a feedback term as per the following relation:

$$\begin{aligned} U_{n+1}(\boldsymbol{\rho}) &= U_n(\boldsymbol{\rho}) && for\,(\boldsymbol{\rho}) \in C \\ &= U_n(\boldsymbol{\rho}) - \beta U_n(\boldsymbol{\rho}) && for\,(\boldsymbol{\rho}) \notin C \end{aligned} \qquad (1.15)$$

here, β is the feedback parameter that controls the convergence properties of the HIO algorithm and values of β is selected from range [0,1].

4. The updated object is Fourier transformed back to the Fourier domain, where the measured modulus replaces the amplitude, and the process repeats.

The negative feedback mechanism in the HIO algorithm significantly improves convergence, especially for complex objects, by preventing stagnation at local minima.

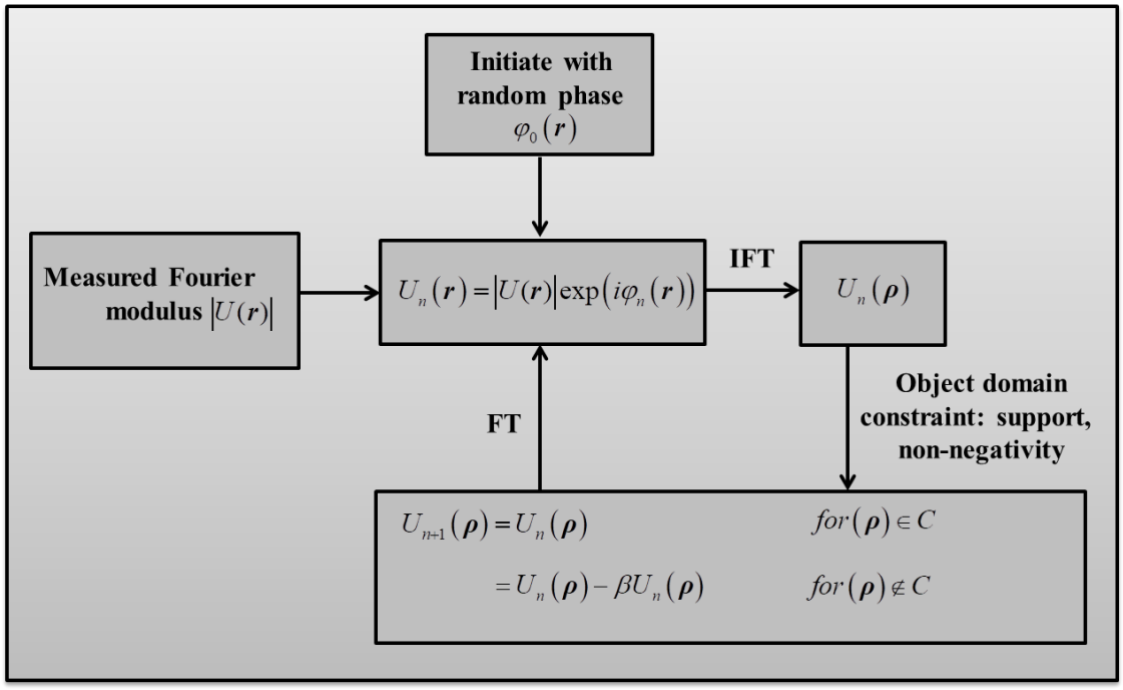

Fig. 1.7 Schematic diagram of HIO algorithm [84].

1.2.2.3 Ptychography

Ptychography is a modern implementation of iterative phase retrieval that combines multiple low-resolution diffraction patterns to reconstruct high-resolution, wide-field images of complex structured samples [94,95,105–110]. Hoppe proposed ptychograhy in 1969 [94] to solve the phase problem in electron diffraction measurements. However, the current form of ptychography was established by Faulkner and Rodenburg [95]. This technique involves overlapping illuminated regions of a sample at varying angles, producing a series of intensity images stitched together using iteration to provide high-resolution phase information. Fourier ptychography has been used to visualize the 3D structures from light scattering signals or complex transmittance functions [108]. Recently, single-shot ptychography is developed, where all intensity patterns are recorded simultaneously on a single detector [109]. This technique uses an array of overlapping probes to create overlapping probes, which are recorded on a single detector. A

ptychographic reconstruction was performed successfully from this data. This method exploits the robustness of ptychography, while avoiding long acquisition times. A schematic of an experimental setup for the conventional scanning and single-shot ptychography is illustrated below in Fig. 1.8.

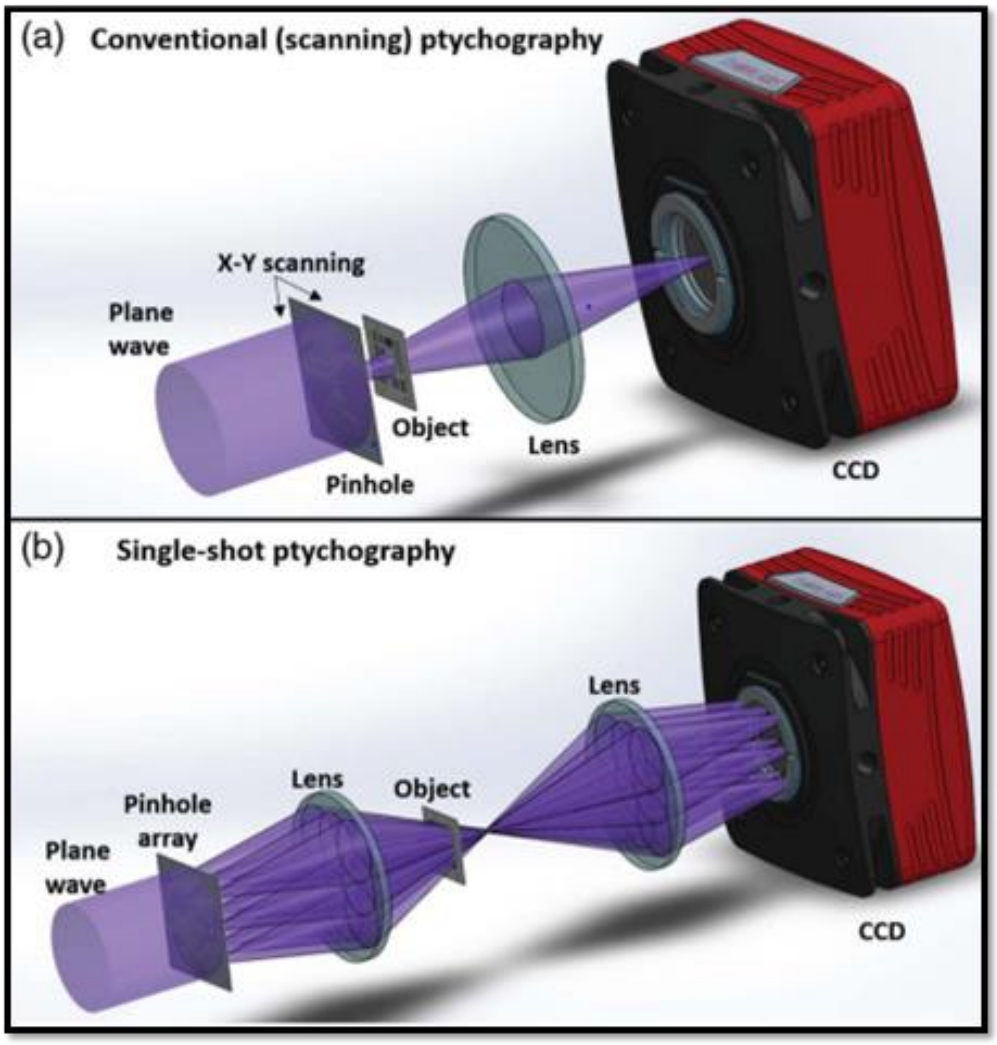

Fig. 1.8 Schematic experimental setups for conventional and single-shot ptychography technique. (a) Conventional (b) Single-shot ptychographical setup [109].

Several other iterative techniques have been developed to recover phase information from the intensity measurements. Some of these iterative methods are the autocorrelation approach [96–98,112], Wigner distribution deconvolution method [99], the use of focus

variation, the parabola method [100,101], scanning a slit aperture [102], aperture array [103], iterations with speckles [104], etc.

1.3 Polarization imaging

Polarization, alongside amplitude and phase, is a fundamental property of light that provides unique opportunities in both fundamental research and applied sciences [24–27]. By revealing intensity differences corresponding to the inherent characteristics of a material, polarization serves as a powerful tool for characterizing the intrinsic properties of objects. As an additional dimension of information, polarization has driven the development of numerous imaging techniques. These techniques can be broadly categorized into intensity-based approaches, such as Stokes vector and Mueller matrix measurements [113–115], and field-based approaches, including Jones matrix detection [116–118]. Field-based Jones matrix techniques have been instrumental in studying anisotropic properties over the last few decades. However, these methods are limited by the requirement for fully polarized light, which restricts their use in certain scenarios. In contrast, Stokes and Mueller formalisms are highly versatile, as they can be applied regardless of the state of polarization (SOP) of light. The concept of Stokes parameters (SPs), introduced by George Gabriel Stokes in 1852 [27], characterizes polarization using four observables and has since become a cornerstone in polarimetric imaging.

For a transversely polarized light field, the SPs are defined as [27]

$$S_m(\boldsymbol{r}) = \boldsymbol{U}^{\dagger}(\boldsymbol{r})\boldsymbol{\sigma}^m\boldsymbol{U}(\boldsymbol{r}), \quad (m=0,1,2,3), \tag{1.16}$$

where, $\boldsymbol{U}(\boldsymbol{r}) = \begin{pmatrix} U_x(\boldsymbol{r}) \\ U_y(\boldsymbol{r}) \end{pmatrix}$, represents the complex field of the polarized light field at a spatial position $\boldsymbol{r}$, and x and y denote the direction of horizontal and vertical polarization

components, respectively, and $\boldsymbol{\sigma}^m$ denotes the identity matrix and three Pauli spin matrices, which are represented as

$$\boldsymbol{\sigma}^0 = \begin{pmatrix} 1 & 0 \\ 0 & 1 \end{pmatrix}, \boldsymbol{\sigma}^1 = \begin{pmatrix} 1 & 0 \\ 0 & -1 \end{pmatrix}, \boldsymbol{\sigma}^2 = \begin{pmatrix} 0 & 1 \\ 1 & 0 \end{pmatrix}, \boldsymbol{\sigma}^3 = \begin{pmatrix} 0 & -i \\ i & 0 \end{pmatrix}, \tag{1.17}$$

SPs illustrate the SOP by a point, and the SOP is geometrically visualized on a polarization ellipse or the Poincare sphere [27] as shown in Fig.1.9.

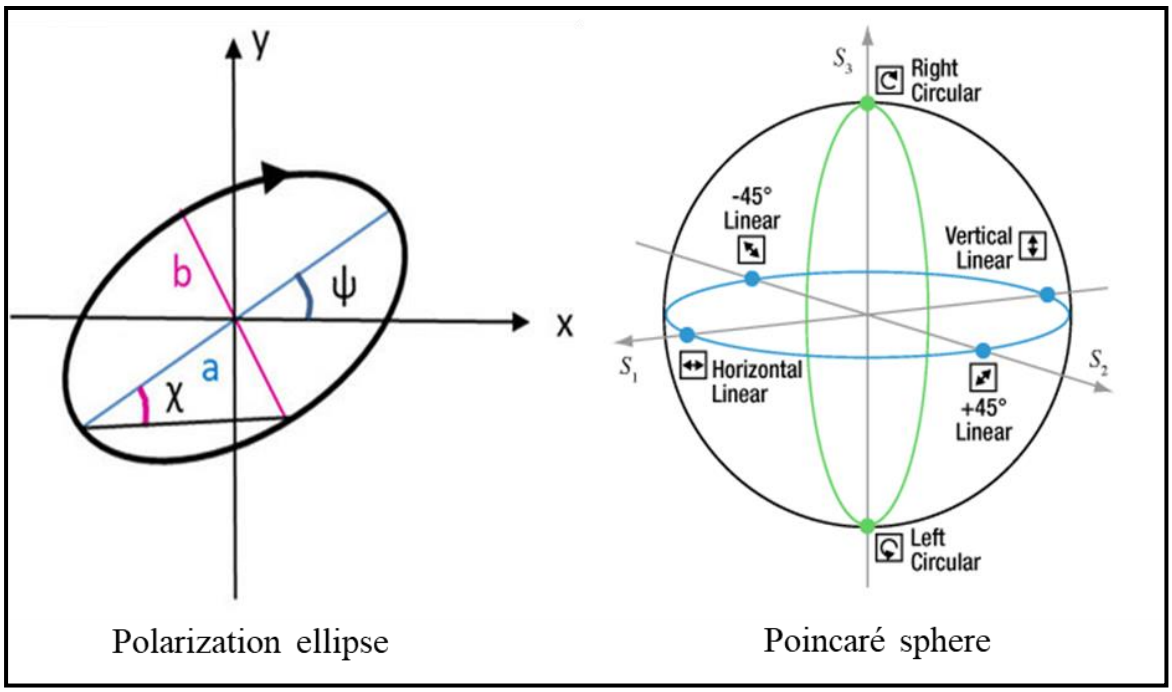

Fig. 1.9 SOP representations through polarization ellipse and Poincare sphere [27].

For polarization imaging, the measurement of all four Stokes parameters is essential. Conventional polarization imaging systems achieve this by employing retarders and polarizers to record four intensity patterns on a detector. A schematic for the experimental measurement of SPs is shown in Fig. 1.10.

For a retarder with phase φ and a linear polarizer with rotation angle θ, the resulting measured intensity $I(\boldsymbol{r},\theta,\varphi)$ can be expressed as a function of these elements' position and the incident beam's SPs, as follows [119]

$$I(\boldsymbol{r},\theta,\varphi)=\frac{1}{2}\left[S_0(\boldsymbol{r})+S_1(\boldsymbol{r})\mathrm{Cos}(2\theta)+S_2(\boldsymbol{r})\mathrm{Sin}(2\theta)\mathrm{Cos}(\varphi)-S_3(\boldsymbol{r})\mathrm{Sin}(2\theta)\mathrm{Sin}(\varphi)\right] \quad (1.18)$$

From equation (8), four measurements of $I(\boldsymbol{r},\theta,\varphi)$ with known θ and φ result in a system of linear equations, from which the SPs can be calculated as

$$\begin{aligned} S_0(\boldsymbol{r})&=I(\boldsymbol{r},0^\circ,0^\circ)+I(\boldsymbol{r},90^\circ,0^\circ),\\ S_1(\boldsymbol{r})&=I(\boldsymbol{r},0^\circ,0^\circ)-I(\boldsymbol{r},90^\circ,0^\circ),\\ S_2(\boldsymbol{r})&=2I(\boldsymbol{r},45^\circ,0^\circ)-S_0(\boldsymbol{r}),\\ S_3(\boldsymbol{r})&=S_0(\boldsymbol{r})-2I(\boldsymbol{r},45^\circ,90^\circ). \end{aligned} \quad (1.19)$$

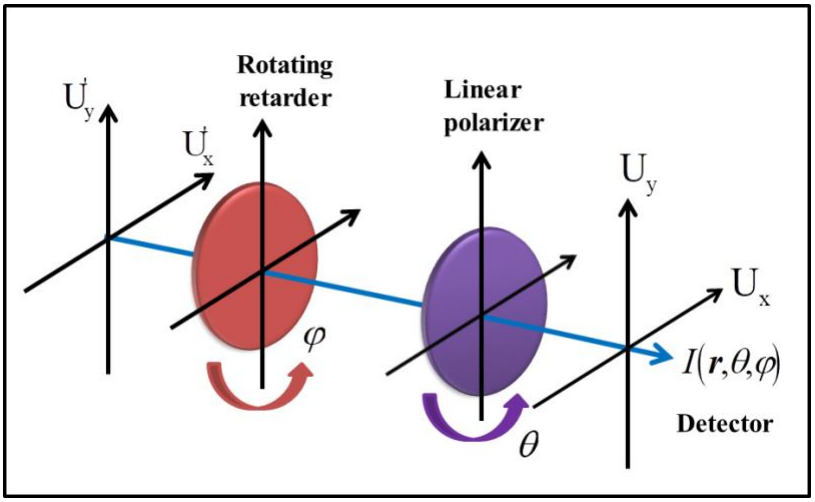

Fig. 1.10 Schematic for the experimental measurement of SPs.

However, these systems require four separate intensity pattern and relying on mechanically rotating optical elements, which introduces experimental limitations. To address these challenges, several other polarization imaging techniques have been developed, utilizing advanced tools such as polarization cameras, digital micromirror

devices (DMDs), and metasurface-based optical elements, etc. [120–130]. These innovations enable faster and more efficient measurements, overcoming the drawbacks of traditional approaches.

Furthermore, polarization imaging has been extended into the DH domain to enable measurement of the SOP of a field [28,131–137]. Various DH configurations, including on-axis, off-axis, and phase-shifting single-shot schemes, have been devised to achieve polarimetric measurements [28,132,138,139]. One such experimental setup is illustrated in Fig. 1.11.

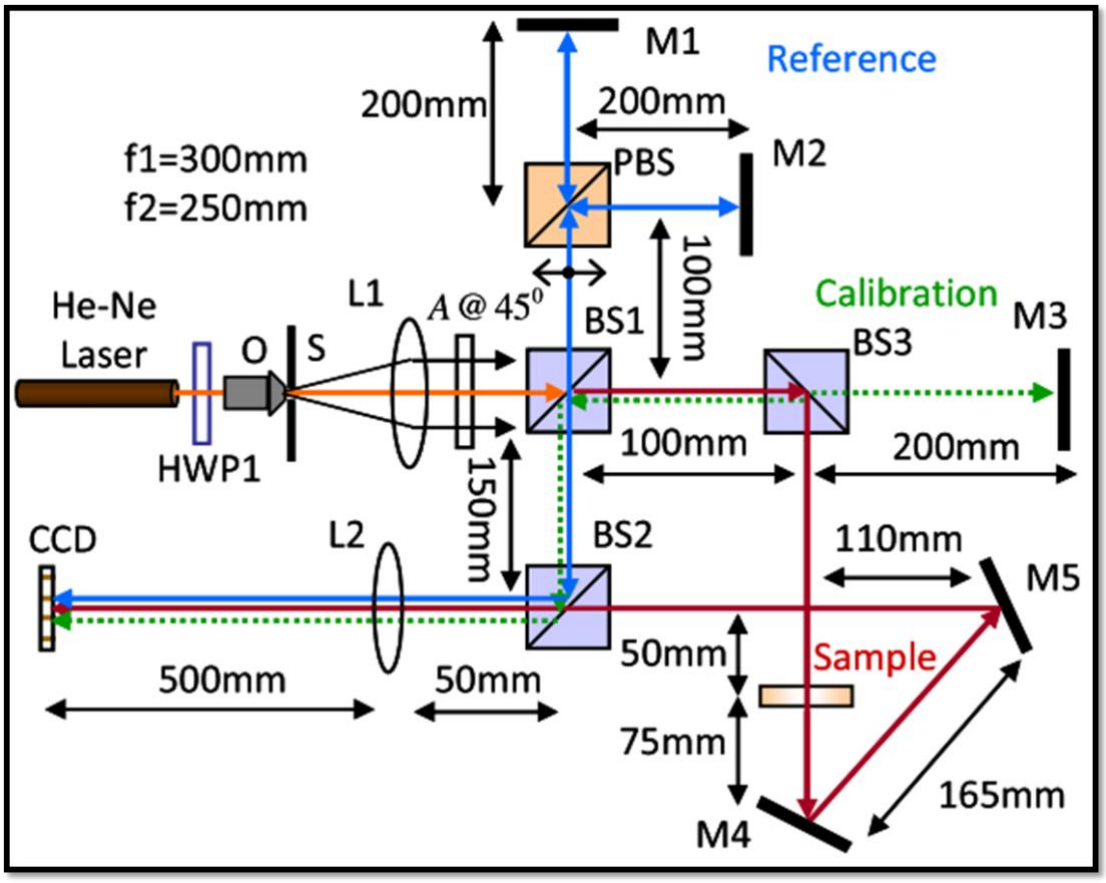

Fig. 1.11 Experimental setup for polarimetric imaging with an integrated calibration scheme [139].

In this interferometric polarization DH configuration, single-shot polarimetric measurement is proposed without using any prior knowledge of the reference beam.

These techniques use integrated calibration schemes to mitigate the errors arising from reference field inaccuracies or spatial carrier frequency artifacts [139].

While these optical imaging techniques discussed above have been successfully implemented in free space and homogeneous media, many real-world applications require imaging through random scattering environments. The following sections explore the challenges and advancements in optical imaging through random scattering media, highlighting their significance in overcoming these barriers.

1.4 Optical imaging with/through randomness

Imaging through random scattering media has long been a longstanding challenge in optics due to disruption of light's wavefront by scattering. Scattering occurs when light is deflected by small particles suspended in a medium with a different refractive index from the surrounding medium.

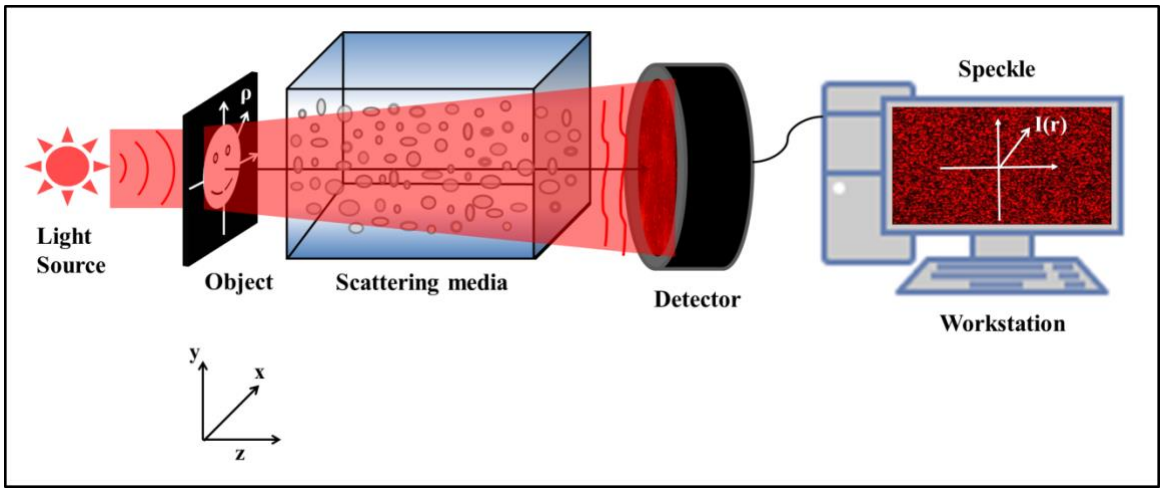

Fig. 1.12 Generation of the speckle pattern.

When a light beam carrying object information is propagated through scattered media or reflects off a rough surface, it produces a scattered wavefront. According to Huygen's principle, each scattered point can be treated as a source of secondary wavelet. Because of the intricate scattering process, the scattered wavefront at any point results from the

coherent summation of multiple wavelets, each with a random phase and amplitude due to varying pathlengths through the scattering media. The coherent summation generates a granular intensity pattern known as a speckle. Hence, the direct information of the object is unavailable at the detector. An example of light incident on an object, then passing through scattering media and generating a speckle pattern is illustrated in Fig. 1.12 [140,141]. This speckle pattern consists of speckle grains with varying intensities arising from the phase differences introduced by height variations in the rough surface. Hence, optical imaging through the diversity of random media, including the presence of fog, atmospheric turbulence, and biological tissues, is practically challenging as each medium introduces unique scattering properties and with the appearance of speckles, direct access to object information is impossible. Fig. 1.13 provides a visualization of imaging through different types of random media [142], highlighting their challenges and opportunities. The grainy structure of these speckle patterns carries subtle signatures of the underlying object information, and proper evaluation and utilization of this scattered light can lead to innovative tools and techniques for optical imaging through scattering media.

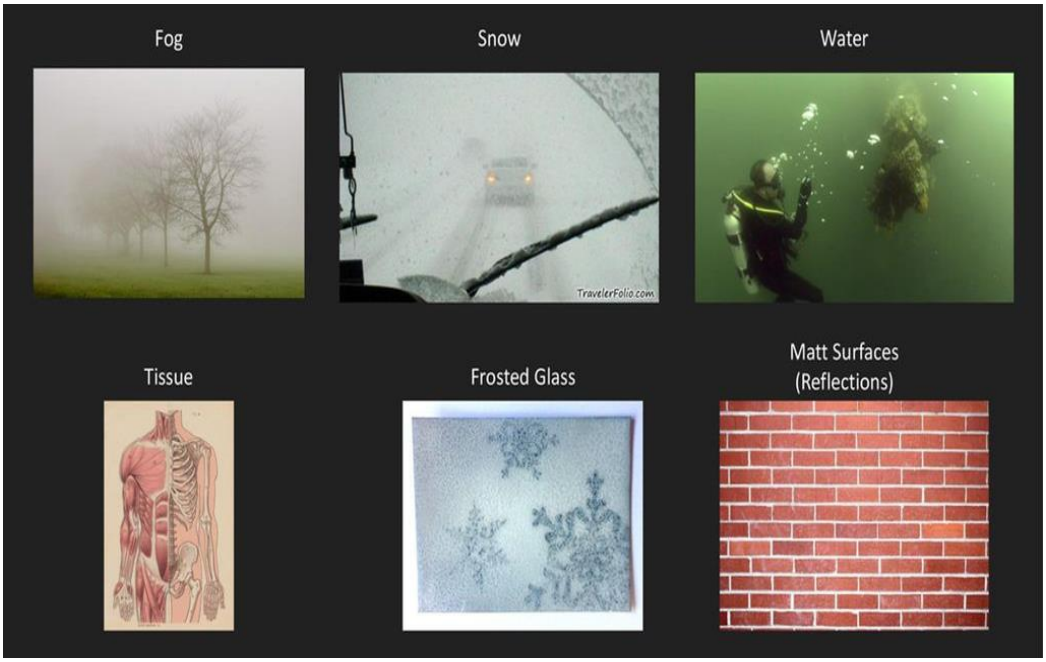

Fig. 1.13 Visualization of imaging through different types of random media [142].

Techniques developed for imaging through scattering media can be broadly categorized into two approaches. The first involves canceling the randomness, while the second leverages the randomness. The former approach includes techniques like adaptive optics [143], optical phase conjugation and wavefront shaping [144–149], transmission matrix [150–152], etc. The latter exploits the correlation properties of scattered light, such as the memory effect [153,154], statistical correlation [155–159], etc. Some key techniques for imaging through random scattering media are discussed below.

1.4.1 Adaptive optics

Adaptive optics (AO) is a technique designed to detect and correct distorted wavefronts caused by scattering media in real time [143]. In this technique, using a wavefront sensor, distorted wavefronts are measured and subsequently corrected by a deformable mirror or other adaptive optical elements. This process typically involves phase conjugation techniques, where the distorted wavefront is reversed and corrected. A closed-loop system continuously feeds wavefront information from the wavefront sensor to a control system, which adjusts the deformable mirror to correct the wavefront of light. A typical AO system for atmospheric turbulence is depicted in Fig. 1.14.

Originally developed for astronomical telescopes, AO has been widely applied in microscopy techniques such as confocal microscopy, two-photon microscopy, etc. to enhance image quality [160]. Despite its success, AO faces challenges, including the complexity and cost of the systems, the requirement of specialized hardware, and the need for extensive computation to correct highly distorted wavefronts. Moreover, the correction of a limited number of modes in the AO is another practical challenge in the strong scattering.

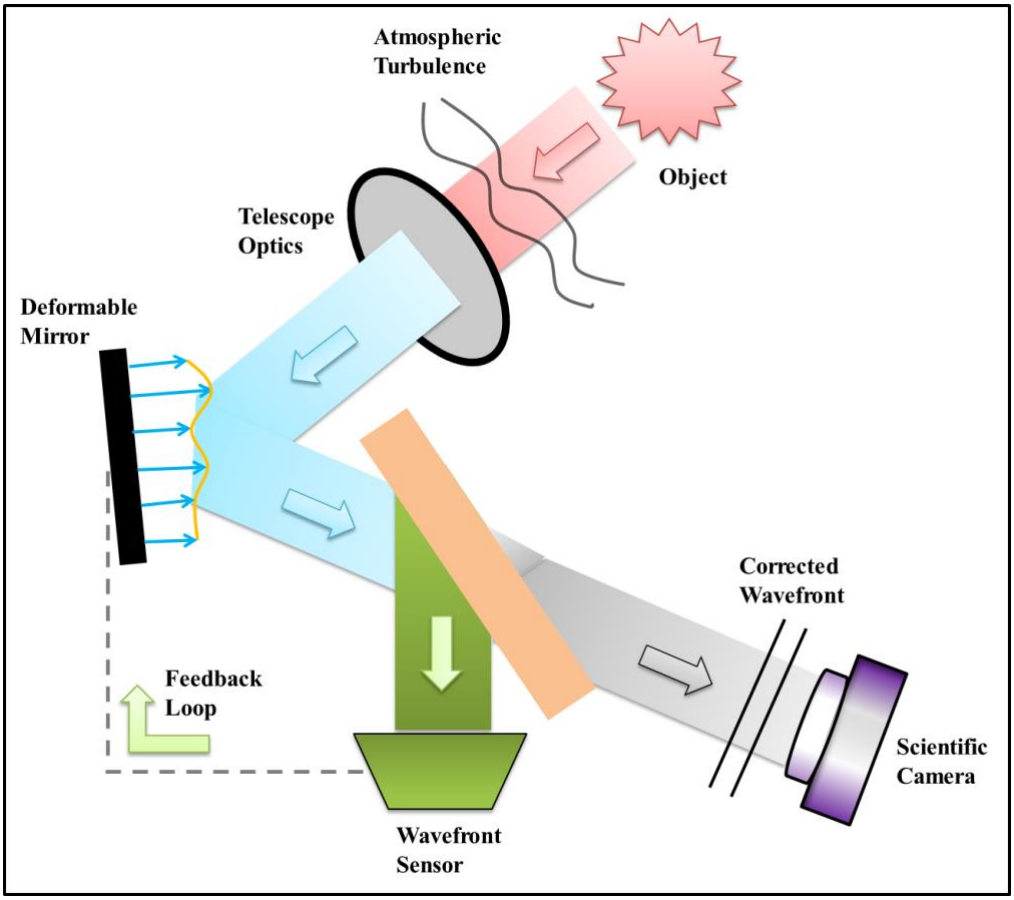

Fig. 1.14 A schematic of the AO approach [21].

1.4.2 Optical phase conjugation

Optical phase conjugation (OPC) reconstructs distorted wavefronts by compensating phase distortions to recover the original wavefront. In OPC, the scattered wavefront is measured outside the scattering medium, phase-conjugated (i.e., its phase is shifted by π) using a phase-conjugated mirror and sent back through the medium. Reciprocity in light propagation ensures the conjugated wave refocuses to its original state after traversing the medium again. A schematic of OPC is shown in Fig. 1.15.

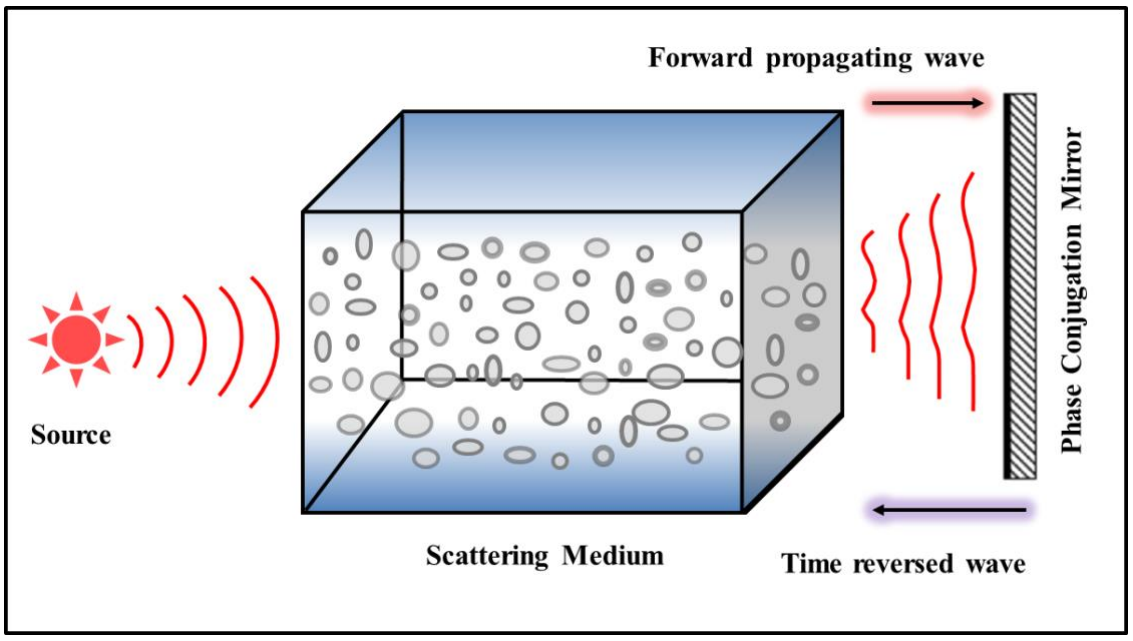

Fig. 1.15 Schematic of OPC [144].

Non-linear optical processes such as four-wave mixing, backward stimulated scattering, and others [161,162] are often employed to generate phase-conjugated waves. Digital phase conjugation has also been reported, combining digital holography with spatial light modulators (SLMs) [163] to achieve fast and precise phase conjugation. While OPC is highly effective for wavefront correction, practical challenges include requiring a non-linear optical process and precise alignment of the optical setup.

1.4.3 Transmission matrix approach

The transmission matrix (TM) method characterizes the linear relationship between the input and output field through scattering media. By monitoring the scattering media's TM, distortions caused by the scattering media can be canceled to a large extent, enabling imaging and focusing through scattering media. Knowledge of TM allows the original image to be reconstructed by applying an inverse matrix operation to the distorted wavefront.

The experimental design to measure TM using devices like SLM is depicted in Fig. 1.16. The TM links the optical fields of n^{th} input-free mode and m^{th} output-free mode by the complex coefficients for a given wavelength through a linear relation $U_m^{out} = \sum_n k_{mn} U_n^{in}$. Once determined, the TM provides the necessary input field to produce any desired output field and thus permits the transmission of images through the scatterer for imaging applications [150–152]. While this approach offers significant advantages, it requires rigorous calibration and precise optical setups with no stray light.

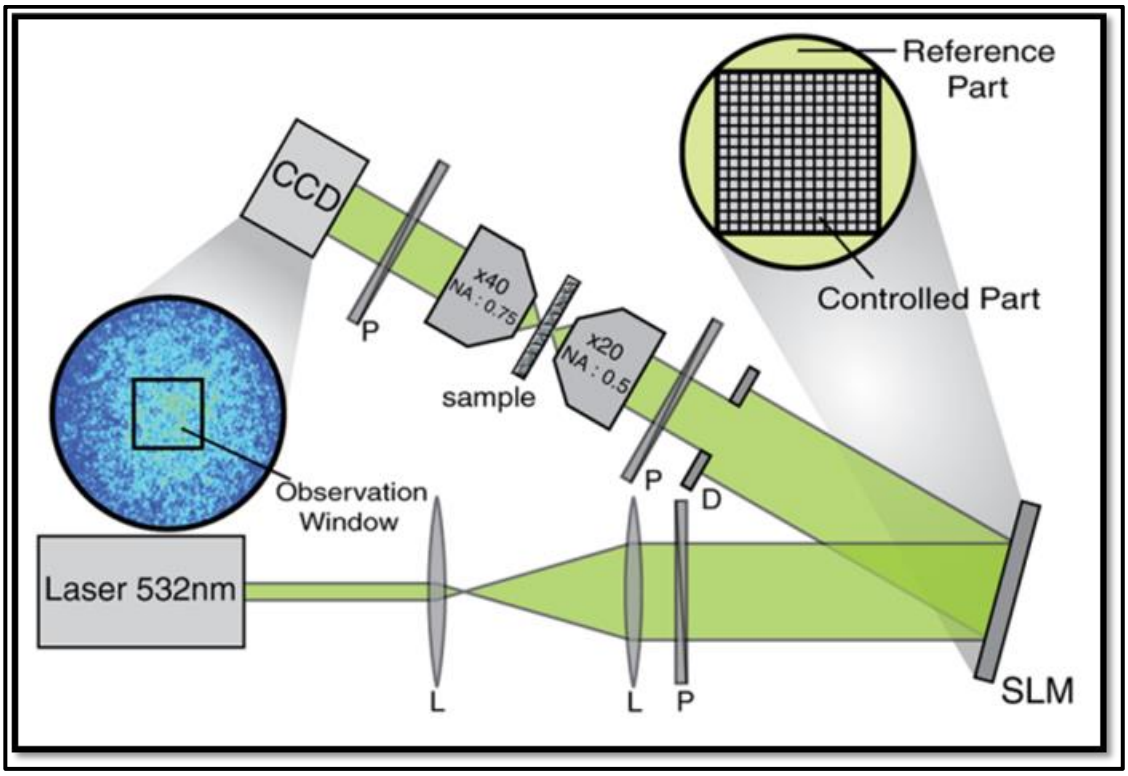

Fig. 1.16 Experimental setup for the measurement of TM [150].

1.4.4 Wavefront shaping

Wavefront shaping (WFS) is a recently developed technique for guiding light through scattering mediums. It manipulates the wavefront of the incident light to counteract scattering effects. WFS employs devices like SLMs or digital micromirror devices (DMDs) to spatially modulate the wavefront [146–149], as shown in Fig. 1.17.

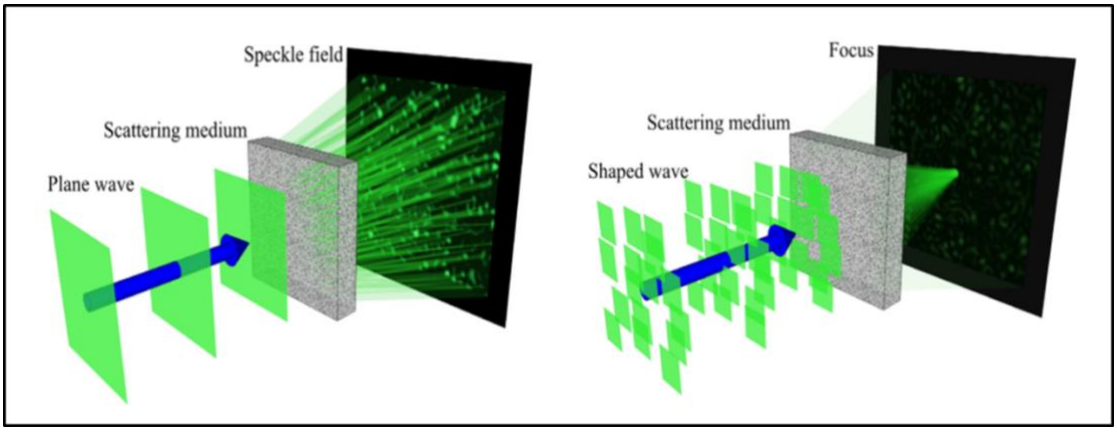

Fig. 1.17 Illustration of focusing through scattering media by wavefront shaping [149].

Using optimization algorithms, the phase of the incident wavefront is iteratively adjusted based on the feedback from the measured intensity at the target location. The power of the wavefront-shaping approach lies in the fact that the SLM can be used both to measure the phase needed to compensate for the scattering and to apply the corresponding correction. WFS is particularly effective for creating a diffraction-limited focus spot through scattering media. However, imaging requires correcting wavefront distortions at multiple points in the desired field of view, necessitating determining numerous wavefront corrections. This makes imaging through scattering media more difficult than single-point focusing.

While the aforementioned techniques focus on the principle of cancellation of randomness, new trends have also emerged utilizing randomness of light rather than cancellation. Among these, the correlation properties of speckle patterns have garnered significant attention. Techniques like memory effect and two-point statistical correlations utilize the statistical features of random light for imaging applications. These methods signify a change in viewpoint, demonstrating that randomness can be a resource for developing novel imaging techniques. A detailed exploration of correlation-based

methods forms the core objective of this thesis, and some of these methods are briefly touched on here.

1.4.5 Correlation optics

Correlation optics has evolved into an exceptionally fascinating and promising domain in modern optics, with diverse applications spanning imaging, communication, astronomy, industrial metrology, etc. Recent advancements and novel illumination sources have inspired researchers to exploit random light and correlation principles for advanced imaging techniques. This section delves into the theoretical foundations and experimental methodologies that leverage correlation optics for imaging through scattering media.

1.4.5.1 Intensity autocorrelation

Using correlations between speckle patterns has paved the way for developing non-invasive imaging systems through scattering media. One notable advantage of speckle-correlation imaging over techniques like the TM and WFS approach is its non-invasive nature. The angular memory effect principle, as articulated by Freund et al. (1988), states that objects angularly separated by a small angle (θ) produce identical speckles at the observation plane, differing only by a lateral shift [153,154]. This principle, depicted in Fig. 1.18, has been instrumental in developing imaging techniques through scattering media [164–167]. By combining the memory effect with intensity autocorrelation, researchers have reconstructed images of objects obscured by random light [166,167]. These techniques employ the intensity speckle pattern with iterative phase retrieval to recover information from the randomness.

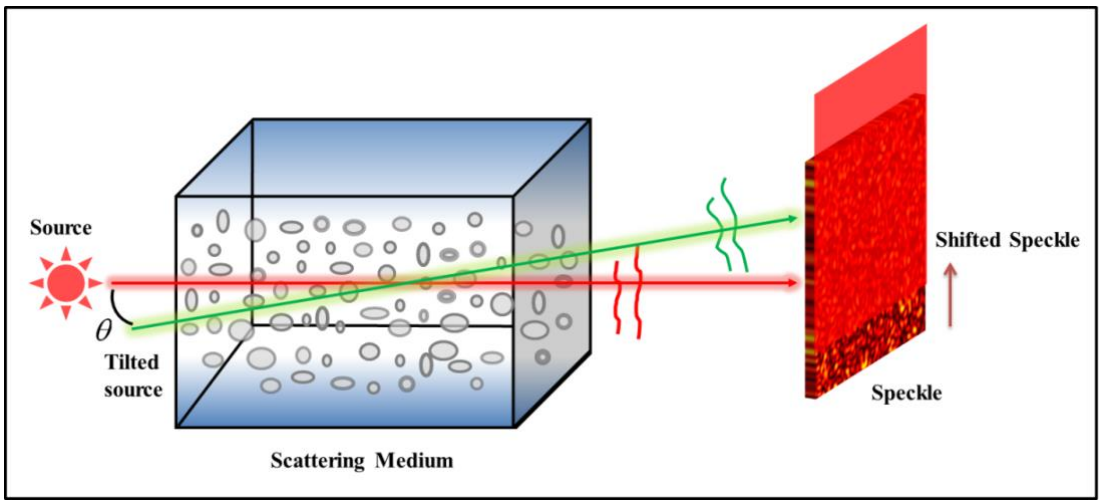

Fig. 1.18 Schematic of the memory effect: an incident-tilted source results in the shift of the speckle pattern.

1.4.5.2 Non-iterative statistical correlation approach

Beyond memory effect-based iterative methods, non-iterative approaches utilizing fundamental features of random light, such as the two-point complex coherence function, offer another avenue for imaging through scattering media. The two-point complex coherence function characterizes spatial or temporal correlations for random light.

Emil Wolf's seminal contributions to coherence optics laid the theoretical background for exploring statistical correlation-based characterization and imaging methods [168]. For instance, the modulus of the two-point complex coherence function has been used in early 20th-century experiments, such as determining the angular diameter of stars using the Michelson stellar interferometer [169]. Although sensitive to external disturbances, this approach inspired subsequent innovations in imaging through the first-order correlation of the field [170,171].

On the other hand, in 1956, Robert Hanbury Brown & Richard Twiss (HBT) introduced intensity interferometry, which uses correlations of the intensity fluctuations to characterize light fields and develop imaging modalities [172–174]. The HBT approach

utilizes the connection between the first and second-order Gaussian random field to determine the angular diameter of stars [172]. Compared to first-order field correlation-based interferometers, HBT interferometers relying on second-order intensity correlations are stable and more robust against external disturbances [175–177]. The HBT approach has led to significant advancements in speckle correlation imaging [175,176,178–180], astronomy, high energy physics, nuclear physics, atomic physics [181], and quantum imaging [182–184].

The mathematical framework underpinning intensity correlations in stochastic light fields is elucidated below [4], along with a sketch diagram in Fig. 1.19.

The instantaneous intensity at the observation plane is represented as

$$I(\boldsymbol{r}) = U^{*}(\boldsymbol{r})U(\boldsymbol{r}) \tag{1.20}$$

where $U(\boldsymbol{r})$ represents the complex field at a spatial position $\boldsymbol{r}$.

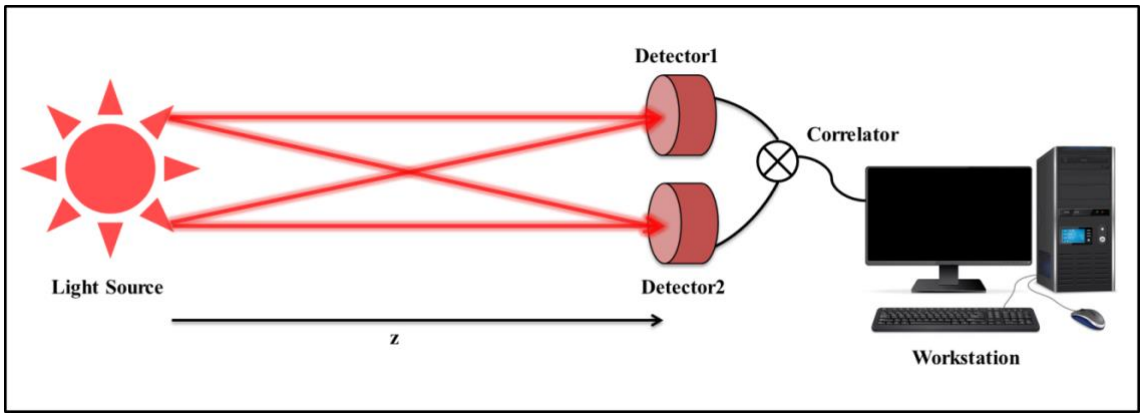

Fig. 1.19 Schematic diagram for intensity correlation measurement.

The first-order correlation function can characterize the statistical property of the stochastic field as

$$W(\boldsymbol{r}_1,\boldsymbol{r}_2)=\left\langle U^*(\boldsymbol{r}_1)U(\boldsymbol{r}_2)\right\rangle, \tag{1.21}$$

where $\boldsymbol{r}_1$ and $\boldsymbol{r}_2$ are the two separate points in space. The angular bracket $\langle ... \rangle$ represents the ensemble average.

The second-order intensity correlation is expressed as

$$\left\langle I(\boldsymbol{r}_1)I(\boldsymbol{r}_2)\right\rangle=\left\langle U^*(\boldsymbol{r}_1)U(\boldsymbol{r}_2)U^*(\boldsymbol{r}_2)U(\boldsymbol{r}_1)\right\rangle. \tag{1.22}$$

Fluctuation in intensity at the observation plane is given by,

$$\Delta I(\boldsymbol{r})=I(\boldsymbol{r})-\left\langle I(\boldsymbol{r})\right\rangle, \tag{1.23}$$

where $\left\langle I(\boldsymbol{r})\right\rangle$ represents the mean intensity. For a Gaussian random field, the second-order correlation can be written in terms of first-order correlation by utilizing the Siegert relation [4] as

$$\left\langle I(\boldsymbol{r}_1)I(\boldsymbol{r}_2)\right\rangle=\left\langle I(\boldsymbol{r}_1)\right\rangle\left\langle I(\boldsymbol{r}_2)\right\rangle+|W(\boldsymbol{r}_1,\boldsymbol{r}_2)|^2, \tag{1.24}$$

Therefore,

$$\left\langle \Delta I(\boldsymbol{r}_1)\Delta I(\boldsymbol{r}_2)\right\rangle=|W(\boldsymbol{r}_1,\boldsymbol{r}_2)|^2 . \tag{1.25}$$

The ensemble average can be realized experimentally by replacing it with either the time average or space average, assuming stationarity and ergodicity. Eq. (1.25) highlights that the second-order correlation can be explained in terms of the modulus of the first-order correlation. Techniques utilizing intensity correlation of the speckle pattern have been demonstrated to develop imaging systems through random scattering media [185]. However, the intensity correlation only provides the amplitude information of the object,

while phase information of the complex coherence function is lost. Recovery of phase in the intensity correlation is possible by combining the holography principle with the interference of coherence waves [135,186–188]. This technique is free from iterations and convergence issues associated with iterative algorithms. An experimental setup for phase recovery using the correlation holography principle is shown in Fig. 1.20 [186]. Here, two statistically independent coherence waves, generated from the object and off-axis reference source, are superposed at the observation plane and are represented as

$$U^s(\boldsymbol{r}) = U(\boldsymbol{r}) + U^R(\boldsymbol{r}) = \int U(\boldsymbol{\rho}) \exp\left(-i\frac{2\pi}{\lambda f}\boldsymbol{r}.\boldsymbol{\rho}\right) d^2\boldsymbol{\rho} + \int U^R(\boldsymbol{\rho}) \exp\left(-i\frac{2\pi}{\lambda f}\boldsymbol{r}.\boldsymbol{\rho}\right) d^2\boldsymbol{\rho}, \quad (1.26)$$

where $\boldsymbol{\rho}, \boldsymbol{r}$, indicate the spatial position vectors at the source and observation planes, respectively, λ represents the incident wavelength, and f is the lens's focal length.

The complex coherence function at the observation plane is represented [186] as

$$W^s(\boldsymbol{r_1}, \boldsymbol{r_2}) = \left\langle U^{s*}(\boldsymbol{r_1}) U^s(\boldsymbol{r_2}) \right\rangle = \left\langle U^*(\boldsymbol{r_1}) U(\boldsymbol{r_2}) \right\rangle + \left\langle U^{R*}(\boldsymbol{r_1}) U^R(\boldsymbol{r_2}) \right\rangle, \quad (1.27)$$

as $\left\langle U^*(\boldsymbol{r_1}) U^R(\boldsymbol{r_2}) \right\rangle \approx 0$, due to the consideration of a statistically independent object and a reference.

Upon substituting the Eq.(1.27) into Eq. (1.25), the right-hand-side of Eq. (1.25) transforms as

$$\left|W^s(\boldsymbol{r_1}, \boldsymbol{r_2})\right|^2 = \left|W(\boldsymbol{r_1}, \boldsymbol{r_2}) + W^R(\boldsymbol{r_1}, \boldsymbol{r_2})\right|^2 \quad (1.28)$$

where, $W^R(\boldsymbol{r_1}, \boldsymbol{r_2}) = \left\langle U^{R*}(\boldsymbol{r_1}) U^R(\boldsymbol{r_2}) \right\rangle$, represents the complex coherence function for the known reference field, respectively. Eq. (1.28) demonstrates the presence of fringes in intensity correlation. The reference coherence function $W^R(\boldsymbol{r_1}, \boldsymbol{r_2})$ covers the support of

the source's coherence function $W(\boldsymbol{r_1}, \boldsymbol{r_2})$ to record the fringes in the intensity correlation. Fourier processing of Eq. (1.28) enables the reconstruction of the source's complex coherence function.

Upon reconstructing the source's complex coherence function, a Fourier transform relation can be established between the object behind the scattering media and the complex coherence function at the observation plane. This relation is derived as follows.

The complex coherence function of the object can be written as

$$W(\boldsymbol{r_1}, \boldsymbol{r_2}) = \int \left\{ \iint U^*(\boldsymbol{\rho_1}) U(\boldsymbol{\rho_2}) \exp\left(-i \frac{2\pi}{\lambda f} (\boldsymbol{r_2}.\boldsymbol{\rho_2} - \boldsymbol{r_1}.\boldsymbol{\rho_1}) \right) d^2\boldsymbol{\rho}_1 d^2\boldsymbol{\rho}_2 \right\} d^2\boldsymbol{r_1}. \qquad (1.29)$$

Making use of the relation $\int \exp\left(-\frac{i2\pi}{\lambda f} (\boldsymbol{\rho_2} - \boldsymbol{\rho}_1).\boldsymbol{r_1} \right) d^2\boldsymbol{r_1} = \delta(\boldsymbol{\rho_2} - \boldsymbol{\rho}_1)$, and for $\boldsymbol{\rho_2} = \boldsymbol{\rho}_1 = \boldsymbol{\rho}$, Eq. (1.29) modifies to

$$W(\boldsymbol{r_1}, \boldsymbol{r_2}) = \int I(\boldsymbol{\rho}) \exp\left(-\frac{i2\pi}{\lambda f} [\boldsymbol{r_2} - \boldsymbol{r_1}].\boldsymbol{\rho} \right) d^2\boldsymbol{\rho}, \qquad (1.30)$$

where, $I(\boldsymbol{\rho}) = U^*(\boldsymbol{\rho}) U(\boldsymbol{\rho})$ represents the intensity of the source.

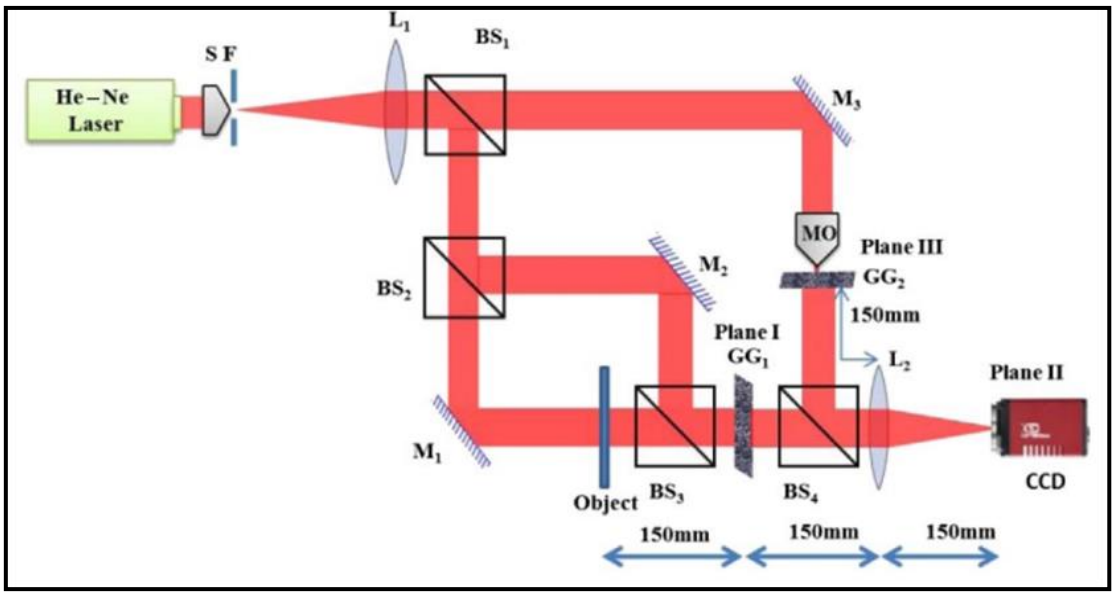

Fig. 1.20 Experimental setup for phase imaging through scattering media using correlation holography [186].

Eq. (1.30) states that the complex coherence function at the observation plane is the Fourier transform of the source at the scattering plane and is known as the van-Cittert Zernike (vCZ) theorem [168].

1.4.6 Correlation for polarized light

Propagation of a coherent polarized light beam through inhomogeneous scattering media generates a coherent random field that exhibits both intensity and polarization fluctuations. Such a coherent random field with polarization fluctuation is termed a polarization speckle [189–191], as represented in Fig. 1.21.

The stochastic nature of the polarized random field necessitates a statistical description of the polarization. In contrast to the two-point correlation in space or time of the random field, referred to as coherence, the polarization of light can be explained using the single-point correlation between two orthogonal polarization components. The unified theory of coherence and polarization [168,192] has spurred great interest in characterizing vector random fields using tools such as the beam coherence–polarization (BCP) matrix (or

cross-spectral density) [168,192], complex degree of coherence [193], generalized Stokes parameters (GSPs) [194], complex degree of mutual polarization [195,196], and degree of polarization in terms of the complex degree of coherence [197], etc.

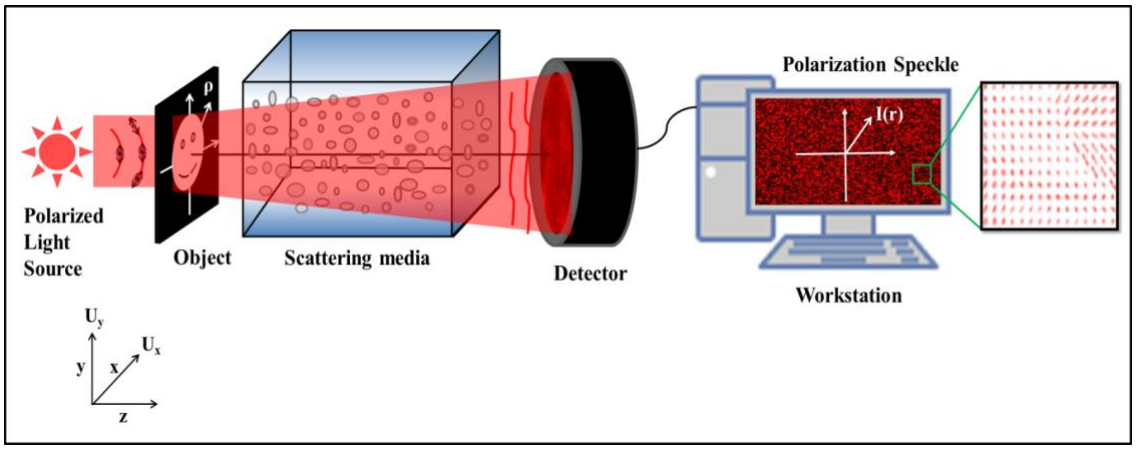

Fig. 1.21 Sketch for generation of polarization speckle. Polarization state distribution in part of the speckle is highlighted on the right-hand side.

The BCP matrix and GSPs offer a comprehensive statistical characterization of vector random fields, facilitating imaging through inhomogeneous scattering media. Hence, developing fast and efficient experimental techniques for measuring the BCP matrix and GSPs of vector light fields is of significant practical importance. In the next section, some experimental techniques for measuring the BCP matrix and GSPs of vector light fields and utilizing them for imaging through randomness are discussed.

1.4.6.1 Beam Coherence–Polarization (BCP) matrix

A BCP matrix is a significant tool for describing statistical features and imaging techniques. The BCP is a 2 × 2 matrix containing two-point correlations among the same or different polarization components at a pair of points in the beam [168,192]. The diagonal elements of the BCP matrix possess the coherence properties of the random light of a random electromagnetic field. In contrast, off-diagonal elements of this matrix are utilized to extract the vectorial features. The BCP matrix is defined as [192]

$$\boldsymbol{W}(\boldsymbol{r_1},\boldsymbol{r_2}) = \begin{bmatrix} \left\langle U_x^*(\boldsymbol{r_1})U_x(\boldsymbol{r_2})\right\rangle & \left\langle U_x^*(\boldsymbol{r_1})U_y(\boldsymbol{r_2})\right\rangle \\ \left\langle U_y^*(\boldsymbol{r_1})U_x(\boldsymbol{r_2})\right\rangle & \left\langle U_y^*(\boldsymbol{r_1})U_y(\boldsymbol{r_2})\right\rangle \end{bmatrix}, \tag{1.31}$$

where, $\left\langle U_p^*(\boldsymbol{r_1})U_q(\boldsymbol{r_2})\right\rangle = W_{pq}(\boldsymbol{r_1},\boldsymbol{r_2}),\ (p,q)=(x,y),$ represents the elements of BCP matrix, and $\boldsymbol{U}(\boldsymbol{r}) = U_x(\boldsymbol{r})\hat{x} + U_y(\boldsymbol{r})\hat{y}$ represents the complex field of the polarized light source at a spatial position $\boldsymbol{r}$, and the angular bracket denotes the ensemble average. Asterisk * represents the complex conjugate, $\boldsymbol{r_1}$ and $\boldsymbol{r_2}$ are the two spatial points. The elements of the BCP matrix may take complex values as they represent the two-point correlation of the orthogonal polarization components of the light field.

Various methods have been developed to measure complex two-point correlation functions relying on first-order intensity in Young's interferometer [198–200]. In these techniques, light passing through two small pinholes interfere with each other to generate an interference pattern, and the resulting interference fringe visibility and fringe phase measure the complex correlation function of the light field. However, the use of tiny pinholes and multiple measurements with varying point source separations are major constraints in Young's interferometric techniques. Therefore, intensive research efforts have been made to overcome these limitations by developing alternative techniques [201–208]. Apart from the interferometry based on first-order intensity, the HBT intensity interferometer based on second-order intensity correlation offers a highly stable experimental configuration to measure the two-point correlation of the light fields. HBT based intensity correlation approach can be extended to the vector light, and a schematic of intensity correlation for vectorial light field is shown in Fig. 1.22.

Let us consider the stochastic polarized light field propagating along the z direction to the observation plane, as shown in Fig. 1.22.

The instantaneous intensity at the observation plane is represented as

$$I(\boldsymbol{r}) = \boldsymbol{U}^{*}(\boldsymbol{r})\boldsymbol{U}(\boldsymbol{r}), \tag{1.32}$$

Fluctuation of the intensities from its mean value is given as

$$\langle \Delta I(\boldsymbol{r}) \rangle = I(\boldsymbol{r}) - \langle I(\boldsymbol{r}) \rangle. \tag{1.33}$$

Under consideration of the Gaussian random process and applying the Siegert relation, the correlation of the fluctuations of the intensities at two points is given as

$$\langle \Delta I(\boldsymbol{r}_1)\Delta I(\boldsymbol{r}_2) \rangle = \sum_{p,q} \left| W_{pq}(\boldsymbol{r}_1, \boldsymbol{r}_2) \right|^2 = tr[\boldsymbol{W}^{\dagger}(\boldsymbol{r}_1, \boldsymbol{r}_2)\boldsymbol{W}(\boldsymbol{r}_1, \boldsymbol{r}_2)] \tag{1.34}$$

where, '*tr*' denotes the trace. Eq. (1.34) highlights that the vectorial extension of intensity correlation involves modulus of all four components of the BCP matrix, and phase information of BCP matrix elements is lost [178].

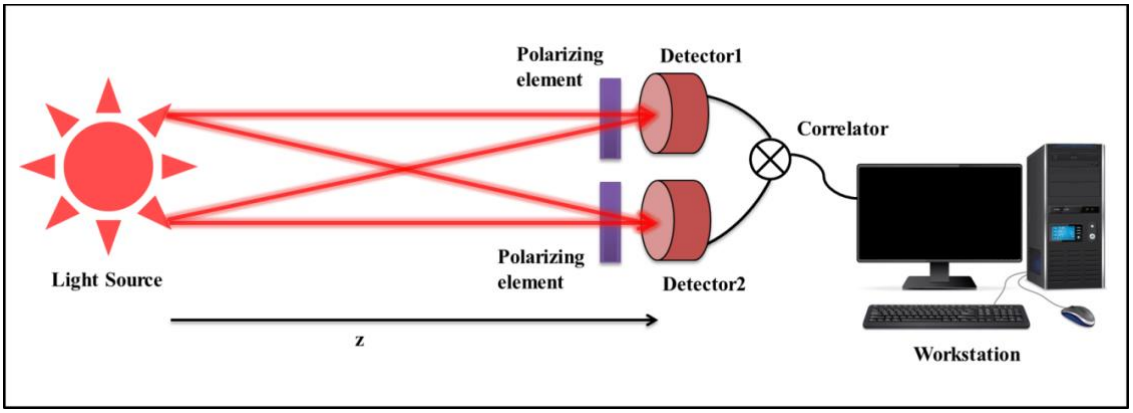

Fig. 1.22 Schematic diagram of intensity correlation of vector field.

To extract the phase information, interferometry within the framework of HBT based intensity correlation is used to develop some unconventional holography techniques to measure the elements of BCP matrix [209,210]. With the help of the elements of BCP matrix, the vector source information can be extracted through vectorial vCZ theorem

[211]. One of the experimental geometries for the imaging of polarized sources through BCP matrix measurement is shown in Fig. 1.23 [212]. In this technique, HBT-based intensity correlation, along with the off-axis holographic principle, has been leveraged for experimentally measuring the BCP and using it for imaging through randomness.

In this experiment, an inhomogeneously polarized beam is synthesized at the observation plane, and with the help of a known reference function, BCP matrix measurement of the synthesized polarized beam is facilitated [212]. In this case, the fluctuation of intensity correlation is expressed as,

$$\langle \Delta I(\boldsymbol{r_1}) \Delta I(\boldsymbol{r_2}) \rangle = \sum_{p,q} \left| W_{pq}(\boldsymbol{r_1}, \boldsymbol{r_2}) \right|^2 = \sum_{p,q} \left| W_{pq}(\boldsymbol{r_1}, \boldsymbol{r_2}) + W_{pq}^{R}(\boldsymbol{r_1}, \boldsymbol{r_2}) \right|^2, \tag{1.35}$$

where, $W_{pq}^{R}(\boldsymbol{r_1}, \boldsymbol{r_2})$ served as a reference. In this technique, to filter individual elements of the BCP matrix, polarizing elements were used before the detector to capture four intensity patterns.

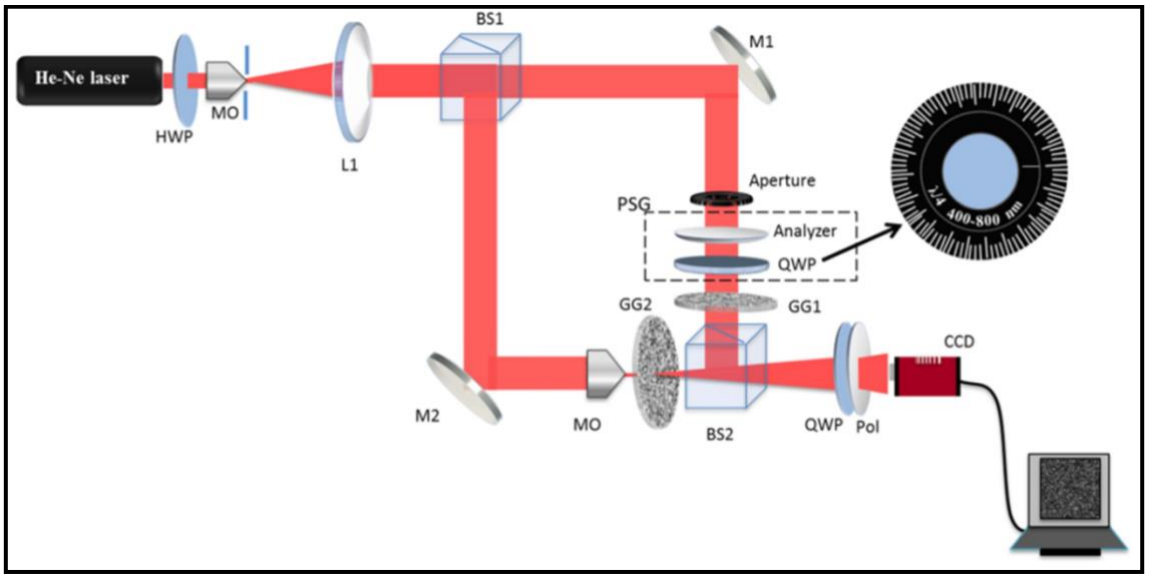

Fig. 1.23 Experimental setup for imaging polarized source behind the scattering media through BCP matrix measurement [212].

Upon reconstruction of elements of the BCP matrix for the synthesized polarized beam, the polarimetric information of the polarized source can be accessed from the elements of the BCP matrix as,

$$I_{pq}(\boldsymbol{\rho}) = \int W_{pq}(\boldsymbol{r_1}, \boldsymbol{r_2}) \exp\left(\frac{i2\pi}{\lambda f}(\boldsymbol{r_2} - \boldsymbol{r_1}).\boldsymbol{\rho}\right) d^2(\boldsymbol{r_2} - \boldsymbol{r_1}), \tag{1.36}$$

where, $I_{pq}(\boldsymbol{\rho}) = U_p^*(\boldsymbol{\rho}) U_q(\boldsymbol{\rho})$ represents the intensity of the orthogonal polarization components of the polarized source.

Moreover, the elements of the BCP matrix have been used to develop some unconventional imaging techniques [213–216]. In another work, Cai et al. have demonstrated a generalized HBT approach by introducing two reference fields with controllable phase delay to measure the elements of the BCP matrix [217].

1.4.6.2 Generalized Stokes Parameters (GSPs)

SPs are fundamental quantity for describing the SOP of a polarized light beam at a point. However, the unified theory of coherence and polarization revealed that the polarization properties of light can evolve as it propagates [194]. To characterize these changes, Olga Korotkova and Emil Wolf extended the concept of single-point SPs to include two-point quantities, introducing GSPs [194]. These GSPs provide a means to analyze how polarization properties change on propagation. These GSPs are expressed in terms of the elements of the BCP matrix as

$$S_m(\boldsymbol{r_1}, \boldsymbol{r_2}) = tr[\boldsymbol{\sigma}^m \boldsymbol{W}(\boldsymbol{r_1}, \boldsymbol{r_2})], \quad \text{(m=0,1,2,3)} \tag{1.37}$$

The GSPs have significantly contributed to both fundamental and applied statistical optics, particularly in the characterization and imaging of stochastic polarized light fields. Traditional methods for measuring GSPs rely on Young's two-pinhole interferometer

combined with retarders and polarizers [218,219]. These setups allow the measurement of polarization fringes with suitable retarders and polarizers, providing coherence and polarization information of the stochastic polarized light field. However, these interferometric techniques are sensitive to environmental vibrations, posing practical challenges. To address these limitations, alternative techniques have been developed. One such technique access the GSPs through two-point intensity correlations [220]. While this technique provides the amplitude information of the GSPs, it does not retain phase information.

Holographic techniques incorporating intensity correlation have been introduced to retrieve both amplitude and phase [221,222]. These methods enable the reconstruction of complex GSPs, facilitating the extraction of polarization properties in scattering environments. Fig. 1. 24 [222] depicts an experimental configuration for measuring the polarization properties from complex GSPs.

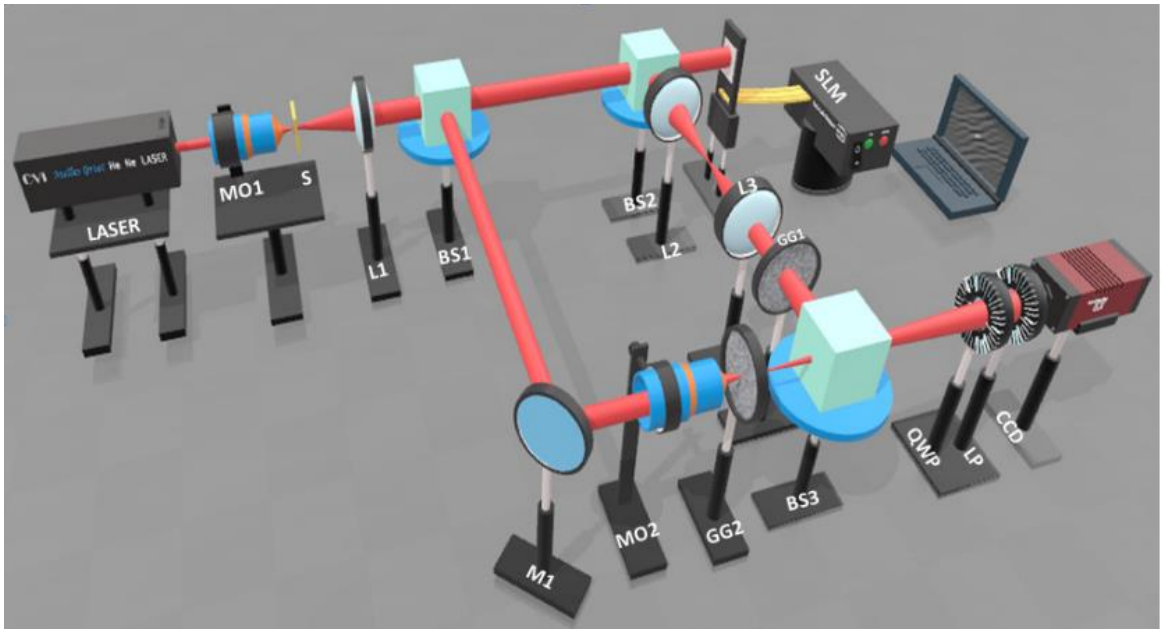

Fig. 1.24 Experimental setup for imaging of polarized source behind the scattering media through GSPs measurements [222].

This technique uses the interference of the GSPs from two independent sources: one from a polarized reference source and another from a to-be-analyzed polarized source. In this case, the intensity correlation is expressed as,

$$\langle \Delta I(\boldsymbol{r}_1)\Delta I(\boldsymbol{r}_2)\rangle = \frac{1}{2}\sum_{m=0}^{3}\left|S_m(\boldsymbol{r}_1,\boldsymbol{r}_2)+S_m^R(\boldsymbol{r}_1,\boldsymbol{r}_2)\right|^2, \tag{1.38}$$

where, $S_m^R(\boldsymbol{r}_1,\boldsymbol{r}_2)$ served as a reference. Further, the reconstruction of GSPs used to retrieve the wavefront of the polarized source from the randomness [222].

1.4.6.3 Polarization correlation

Besides the intensity correlation, polarization correlation provides a robust framework for exploring the statistical properties of stochastic light fields. Visser et al. demonstrated that polarization correlation explores all possible correlations among the four SPs [223,224], broadening the scope of imaging through randomness. Under the assumptions of Gaussian statistics, where these SPs correlations can be expressed in terms of the two-point field correlations [223,224].

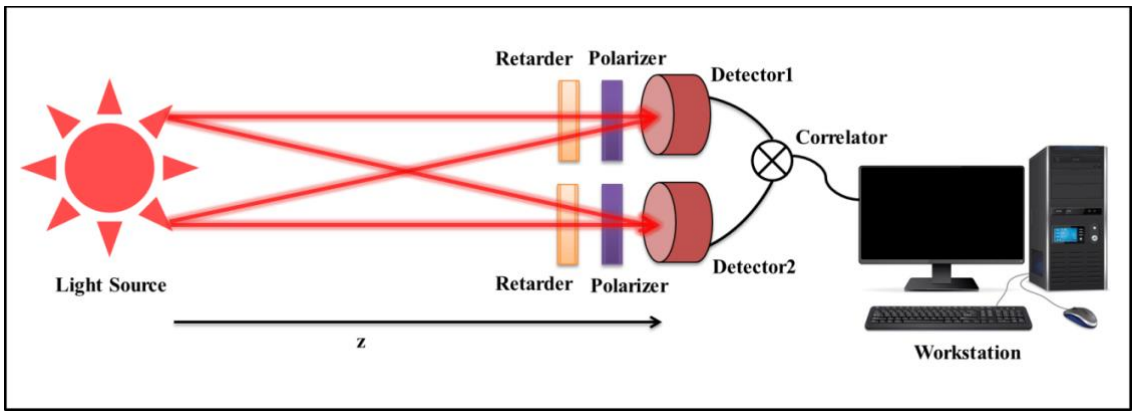

Fig. 1.25 Schematic diagram for the polarization-resolved HBT experiment.

Fig. 1.25 shows a schematic diagram for evaluating the polarization correlation. Polarizing elements, such as a retarder, polarizer, etc. are placed before the two detectors

to analyze the SOP of the light field. A theoretical framework to evaluate polarization correlation is given below.

Fluctuations in SPs at the observation plane are represented as

$$\Delta S_m(\boldsymbol{r}) = S_m(\boldsymbol{r}) - \langle S_m(\boldsymbol{r}) \rangle, \tag{1.39}$$

where S_m indicates the four SPs of the stochastic field at the observation plane and $\langle S_m(\boldsymbol{r}) \rangle$ represents the mean SPs. A correlation between fluctuations in SPs provides information about the polarization of the incident light field. All possible pairs of two-point correlations of fluctuations in SPs are evaluated by a 4x4 Stokes fluctuations correlation matrix elements as

$$C_{mn}(\boldsymbol{r_1}, \boldsymbol{r_2}) = \langle \Delta S_m(\boldsymbol{r_1}) \Delta S_n(\boldsymbol{r_2}) \rangle, \qquad \text{(m, n=0,1,2,3)}, \tag{1.40}$$

Under the consideration of Gaussian statistics, the elements of the matrix are expressed as

$$C_{mn}(\boldsymbol{r_1}, \boldsymbol{r_2}) = tr\left[\boldsymbol{\sigma}^m \boldsymbol{W}^{\dagger}(\boldsymbol{r_1}, \boldsymbol{r_2}) \boldsymbol{\sigma}^n \boldsymbol{W}(\boldsymbol{r_1}, \boldsymbol{r_2}) \right], \tag{1.41}$$

All the sixteen elements of the matrix from Eq. (1.41) are represented as

$$\boldsymbol{C}(\boldsymbol{r_1}, \boldsymbol{r_2}) = \begin{pmatrix} C_{00}(\boldsymbol{r_1}, \boldsymbol{r_2}) & C_{01}(\boldsymbol{r_1}, \boldsymbol{r_2}) & C_{02}(\boldsymbol{r_1}, \boldsymbol{r_2}) & C_{03}(\boldsymbol{r_1}, \boldsymbol{r_2}) \\ C_{10}(\boldsymbol{r_1}, \boldsymbol{r_2}) & C_{11}(\boldsymbol{r_1}, \boldsymbol{r_2}) & C_{12}(\boldsymbol{r_1}, \boldsymbol{r_2}) & C_{13}(\boldsymbol{r_1}, \boldsymbol{r_2}) \\ C_{20}(\boldsymbol{r_1}, \boldsymbol{r_2}) & C_{21}(\boldsymbol{r_1}, \boldsymbol{r_2}) & C_{22}(\boldsymbol{r_1}, \boldsymbol{r_2}) & C_{23}(\boldsymbol{r_1}, \boldsymbol{r_2}) \\ C_{30}(\boldsymbol{r_1}, \boldsymbol{r_2}) & C_{31}(\boldsymbol{r_1}, \boldsymbol{r_2}) & C_{32}(\boldsymbol{r_1}, \boldsymbol{r_2}) & C_{33}(\boldsymbol{r_1}, \boldsymbol{r_2}) \end{pmatrix}. \tag{1.42}$$

Specific combinations of the elements of the Stokes fluctuations correlation matrix, as described by Eq. (1.42), can be used for statistical characterization, polarization imaging methods, etc. Details of some of these techniques will be discussed in the upcoming chapters.

The forthcoming chapters of this thesis delve into the development of quantitative imaging techniques through randomness. Randomness manifests in various forms, including static environments like static scattering walls or biological tissues and dynamic environments like fog or atmospheric turbulence. Correlation-based techniques leverage the physics of randomness, as described by statistical optics, to extract information from randomness. The optical field's randomness is characterized by the concept of ensemble average, a cornerstone of statistical optics.

For dynamic light fields, ensemble average is practically supplanted by time averaging, assuming the stationarity and ergodicity of the stochastic field over time [4]. In contrast, for static scattering scenarios, i.e., for spatially fluctuating light fields, ensemble average is replaced by spatial averaging, considering the statistical field to be stationary and ergodic in space [225].

This thesis explores both static and dynamically fluctuating speckle patterns, developing correlation-based characterization and imaging techniques. This thesis focuses on statistical correlation analysis along with holography principles to develop some characterization and quantitative imaging techniques through static and dynamic scattering media. The outcomes of this research have significant implications for various practical applications, and some of these applications are listed in Fig. 1.26.

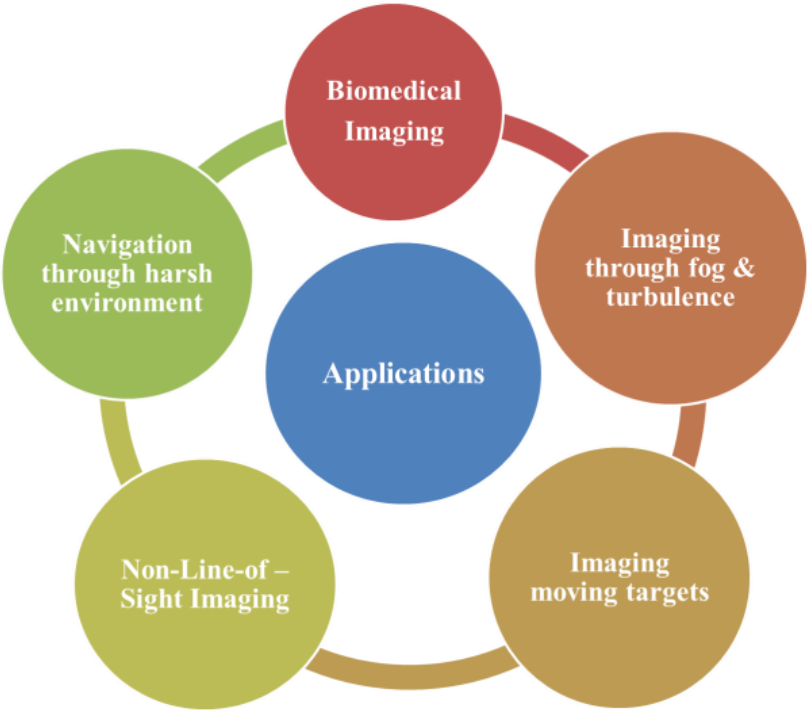

Fig. 1.26 Applications of imaging through randomness using correlation optics.

Fig. 1.27 provides a pictorial overview of the overall thesis contributions, and detailed methodologies and results are discussed in the next chapters.

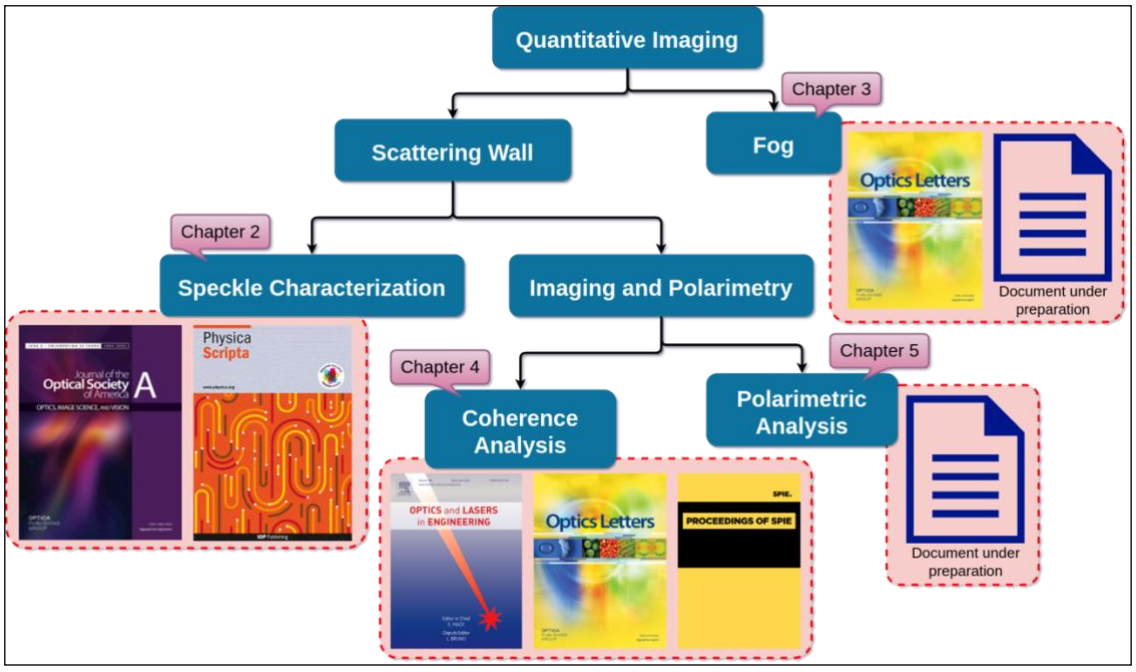

Fig. 1.27 A pictorial overview of the thesis contributions